Bioactive Materials 27 (2023) 488–504

Contents lists available at ScienceDirect

Bioactive Materials

journal homepage: www.keaipublishing.com/en/journals/bioactive-materials

A drug-loaded composite coating to improve osteogenic and antibacterial properties of Zn–1Mg porous scaffolds as biodegradable bone implants

Zhenbao Zhang [a,1], Aobo Liu [b,d,1], Jiadong Fan [a,1], Menglin Wang [a,c], Jiabao Dai [b,d], Xiang Jin [a], Huanze Deng [a,c], Xuan Wang [a], Yijie Liang [a], Haixia Li [g], Yantao Zhao [a,e,f,***], Peng Wen [b,d,**], Yanfeng Li [a,c,*]

[a] Department of Stomatology, the Fourth Medical Center of PLA General Hospital, Beijing, 100048, China
[b] State Key Laboratory of Tribology in Advanced Equipment, Beijing, 100084, China
[c] Medical School of Chinese PLA, Beijing, 100039, China
[d] Department of Mechanical Engineering, Tsinghua University, Beijing, 100084, China
[e] Senior Department of Orthopedics, the Fourth Medical Center of PLA General Hospital, Beijing, 100048, China
[f] Beijing Engineering Research Center of Orthopedics Implants, Beijing, 100048, China
[g] Institute of Process Engineering, Chinese Academy of Sciences, Beijing, 100190, China

ARTICLE INFO

Keywords:
Additive manufacturing
Biodegradable metal
Zn–Mg alloy
Porous scaffold
Composite coating
Bone repair

ABSTRACT

Zinc (Zn) alloy porous scaffolds produced by additive manufacturing own customizable structures and biodegradable functions, having a great application potential for repairing bone defect. In this work, a hydroxyapatite (HA)/polydopamine (PDA) composite coating was constructed on the surface of Zn–1Mg porous scaffolds fabricated by laser powder bed fusion, and was loaded with a bioactive factor BMP2 and an antibacterial drug vancomycin. The microstructure, degradation behavior, biocompatibility, antibacterial performance and osteogenic activities were systematically investigated. Compared with as-built Zn–1Mg scaffolds, the rapid increase of Zn^{2+}, which resulted to the deteriorated cell viability and osteogenic differentiation, was inhibited due to the physical barrier of the composite coating. *In vitro* cellular and bacterial assay indicated that the loaded BMP2 and vancomycin considerably enhanced the cytocompatibility and antibacterial performance. Significantly improved osteogenic and antibacterial functions were also observed according to *in vivo* implantation in the lateral femoral condyle of rats. The design, influence and mechanism of the composite coating were discussed accordingly. It was concluded that the additively manufactured Zn–1Mg porous scaffolds together with the composite coating could modulate biodegradable performance and contribute to effective promotion of bone recovery and antibacterial function.

1. Introduction

Large volume of bone loss caused by trauma, infection, tumor resection, and other injuries can exceed the body's self-repair ability and lead to serious bone defects [1]. Autogenous bone grafting has been the "gold standard" for repairing bone defects [2,3]. However, autologous bone grafting inevitably involves pain, infection and hematoma during bone harvesting at the donor site [4]. Hence, bone repair materials, including bioactive ceramics, polymers, biomedical metals and their composites, have been developed to repair bone defect [5]. Among them, bioactive ceramics and polymers cannot provide sufficient mechanical support for load-bearing applications [6]. Conventional biomedical metals, such as titanium (Ti), tantalum and stainless steel can provide stable mechanical support and have been widely used in clinical applications. However, their non-biodegradable existence as well as stress-shielding effect inhibits the recovery of natural bone and

Peer review under responsibility of KeAi Communications Co., Ltd.
* Corresponding author. Department of Stomatology, the Fourth Medical Center of PLA General Hospital, Beijing, 100048, China.
** Corresponding author. State Key Laboratory of Tribology in Advanced Equipment, Beijing, 100084, China.
*** Corresponding author. Department of Stomatology, the Fourth Medical Center of PLA General Hospital, Beijing, 100048, China.
E-mail addresses: userzyt@qq.com (Y. Zhao), wenpeng@tsinghua.edu.cn (P. Wen), 949427779@qq.com (Y. Li).
[1] These authors contributed equally: Zhenbao Zhang, Aobo Liu, Jiadong Fan.

https://doi.org/10.1016/j.bioactmat.2023.04.017
Received 17 February 2023; Received in revised form 6 April 2023; Accepted 17 April 2023

causes many concerns [7].

Biodegradable metals, which own adequate mechanical properties and can pass through or be metabolized or assimilated by cells and/or issues through gradual degradation in body fluid, have been investigated as promising candidates for orthopedic implants to repair bone defect [8–10]. Nevertheless, the modulation of degradable rate and product has been a critical issue, since the degradation rate should match the term required for bone reconstruction and the degradation product should have no negative effect. For instance, Magnesium (Mg) alloys have been widely studied for biodegradable bone implants, attributing to their moderate strength, excellent biocompatibility and osteogenic activity [11–14]. But, the rapid degradation rate and the release of hydrogen gas significantly limit their applications [15]. Although many measures, such as alloying design, surface modification and the preparation of Mg matrix composites, have been utilized to inhibit the degradation, the rapid degradation of Mg has not been satisfactorily addressed yet [16–20].

In recent years, Zinc (Zn) alloys have attracted widespread attention as promising alternatives to biodegradable Mg alloys [21–25]. Zn is an essential life element, and Zn^{2+} can stimulate the proliferation and differentiation of osteoblast cells by up-regulating runt-related transcription factor 2 (Runx2) expression and alkaline phosphatase (ALP) activity [26,27]. *In vivo* animal studies have confirmed that biodegradable Zn implants promoted new bone formation compared with Ti implants [28]. More importantly, compared to Mg, Zn has a moderate degradation rate and doesn't produce hydrogen gas [29]. The addition of various alloying elements has been attempted to increase the mechanical strength of Zn alloys [29–35]. Among them, adding Li is the most effective, followed by adding Mg. Meanwhile, Mg and Li obviously prompt the proliferation ratio of bone cell, which amazingly reaches 130–180% after 4 days of cultivation [35]. Still, the elastic modulus of Zn alloys is much higher than that of bone. Direct implantation results to stress shielding effect. Furthermore, the complete degradation of Zn alloys is assumed to take 20 months or even longer, which apparently needs to be accelerated considering that the recovery of bone defects normally requires 3–6 months [36,37]. Last but not the least, bone is a hierarchical heterogeneous anisotropic material, whose structure and properties are closely related to different populations and implant sites. It is difficult to match the mechanical property and degradation behavior of Zn alloys to the specific need of patients just by alloying design.

Porous scaffolds produced by additive manufacturing provide freedom to modulate mechanical and degradable performance of biodegradable metal implants [38]. The customized porous structure fabricated by laser powder bed fusion (L-PBF) endows Zn alloy porous scaffolds with adjustable strength and rigidity to match bone as well as accelerated degradation owing to the enlarged surface area and improved permeability [39]. The interconnected pores provide spaces for the in-growth of new bone and blood vessels and enhance the transport of nutrients and metabolic waste [40]. The good fusion quality and refined grain structure contribute to enhanced strength of Zn alloys fabricated by L-PBF. Qin and Wen et al. [41,42] reported that the ultimate tensile strength of pure Zn and Zn–1Mg L-PBF bulks reached 133 and 381 MPa, respectively. The compressive strength and elastic modulus of Zn alloy porous scaffolds were equivalent to those of cancellous bone when the appropriate porosity was obtained. The weight loss of Zn-0.7Li porous scaffolds was 2.60%, roughly 4.6 times that of bulk counterparts after 28-day immersion in Hank's solution. The better cell adhesion and viability were found on porous samples in contrast with bulk samples [39].

Xia et al. [43]. first implanted pure Zn scaffolds fabricated by L-PBF into rabbit femur to repair bone defect of a critical size. After 24 weeks of implantation, the residual volume was approximately 91 ± 0.68%. New bone was observed around the porous scaffold, indicating bone ingrowth and close connection. Qin et al. [42]. used the same animal model and compared the *in vivo* behaviors between pure Zn and Zn–1Mg porous scaffolds. At week 12 after implantation, the fibrous connective tissue remained in pure Zn group. While, Zn–1Mg scaffolds were in tight contact with the surrounding bone, indicating better osseointegration. However, only the bone ingrowth around scaffolds was observed in both groups, and the volume of new bone was limited even after 12 or 24 weeks of implantation. Several *in vitro* studies confirmed that the cell viability and the early osteogenic ability substantially were related to the concentration of released Zn^{2+} from implants [28,30]. For example, when Zn^{2+} concentration was greater than 80 μM/L, prominent toxicity was found in cultures of mouse fibroblasts and osteosarcoma cells [44]. The addition of Mg improved the biocompatibility of Zn alloys by inhibiting the release of Zn^{2+} [29]. However, the significantly enlarged surface of porous scaffolds resulted to an excessive release of Zn^{2+}, which could be the reason of deteriorated osteoblast functionalization especially at the early stage of implantation. Therefore, it is crucial to modulate the degradation and the release of Zn^{2+} for Zn alloy porous scaffolds.

To date, several surface modification methods have been developed to improve the biodegradable performance of Zn alloys [45–47]. Yuan et al. decreased the corrosion rate of Zn-0.1Li alloy by adopting ZrO_2 coating, thus enhancing the biocompatibility *in vitro* and *in vivo* [46]. Zhuang et al. improved the biocompatibility of Zn–3Cu–1Mg porous scaffolds by coating brushite [47]. However, it is still a challenge to prepare uniform and dense coating on the surface of pores for porous scaffolds. Molecular self-assembly allows polymer molecules to be uniformly anchored on the inner and outer surfaces of the porous structure and forms a self-assembled molecular layer bonded to the substrate [48]. Polydopamine (PDA) is a typical polymer for self-assembled coatings and can adhere to the surface of most biomaterials, regardless of their size and shape [49]. Moreover, the PDA coating can act as a bridge to further react with other compounds to form a composite coating. The PDA-induced hydroxyapatite (HA) composite coating significantly reduced the corrosion rate of Mg alloys [50]. Furthermore, both PDA and HA coating can be used as a carrier of drug delivery system, loaded with drug molecules, including antibiotics and growth factors, through chemical bonding or physical adsorption, to customize the biological function of the coating [49,51]. To the author' knowledge, there is no information on the application of drug-loaded composite coatings to Zn alloys porous scaffolds, although this method can give great flexibility to modulate the biodegradable performance and biological function.

In this work, Zn–1Mg porous scaffolds were additively manufactured by a customized L-PBF process, and then were coated with HA/PDA composite by a molecular self-assembly process. Meanwhile, vancomycin (Van) was anchored by PDA coating to enhance the antibacterial property, and BMP2 growth factor was to load in HA coating to further promote the osteogenic activity. The *in vitro* and *in vivo* performances, including biodegradation behaviors, biocompatibility, osteogenesis, and antibacterial properties of coated Zn–1Mg scaffolds were systematically studied. By equipping with the drug-loaded composite coating, Zn–1Mg porous scaffolds were endowed with enhanced osteogenic and antibacterial properties, and thus were more promising for the repair of large-scale bone defect.

2. Materials and methods

2.1. Sample preparation

Cast Zn–1Mg alloy rods (Hunan Institute of Rare Earth Metal Materials, China) were atomized to powders with nitrogen (Nanoval, Germany). The size distribution of powders was 15–53 μm. The content of the Mg element in powders was 1.001 ± 0.004 wt%, measured by inductively coupled plasma optical emission spectrometer (ICP-OES, iCAP6300, USA). The powder morphology and elemental distribution were observed by scanning electron microscope (SEM, Zeiss, Germany) equipped with energy dispersive spectrometer (EDS, Ametek, USA). As shown in Fig. 1a, most of Zn–1Mg powders were spherical, indicating

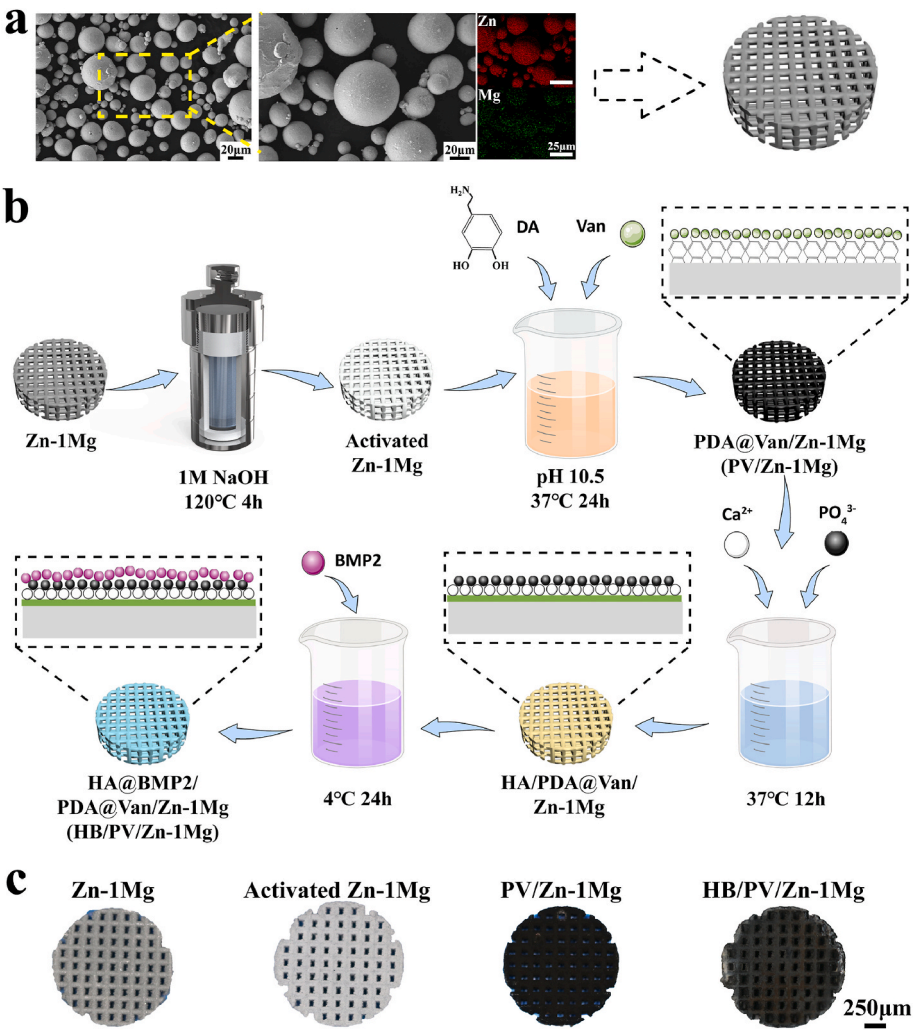

Fig. 1. Sample preparation: (a) Morphology and element distribution of Zn–1Mg powder, and the designed porous scaffold model; (b) Schematic diagram of preparation process; (c) Overview pictures of samples.

good flowability, which was crucial for maintaining the stable formation quality. Moreover, EDS results shown that Mg element was uniformly distributed in particles, helpful for obtaining homogeneous microstructure. A laboratory L-PBF machine (BLT S210, China) was used to fabricate porous samples. The designed scaffolds had a pore size of 600 μm, a pore interval of 450 μm and the porosity of 63.55% (Fig. 1a). The optical system of the machine consisted of a single-mode ytterbium fiber laser (IPG YLR-500, Germany) with a laser spot diameter of 70 μm at the wavelength of 1070 nm. The process was performed in an argon-shielded chamber with an oxygen content less than 100 ppm. The key parameters in the L-PBF process include laser power P_L, scanning speed V_S, hatching space H_S, and layer thickness D_S. Based on the pre-experimental results, processing parameters were set as P_L = 20 W, V_S = 500 mm/s, H_S = 50 μm, and D_S = 30 μm.

As-built Zn–1Mg samples were ultrasonically cleaned and polished by chemical methods (H_2SO_4 3 ml/L, 30% H_2O_2 70 ml/L) to remove residual powders. Subsequently, samples were placed in a hydrothermal kettle with 1 M NaOH, and placed in an oven at 120 °C for 4 h. The obtained samples were recorded as activated Zn–1Mg. The ethanol/ultrapure water (30%) solution was utilized to prepare the PDA coating deposition solution containing Van. The activated Zn–1Mg samples was suspended in the deposition solution, which was composed of 2 mg/mL dopamine (DA, Aladdin, China), 2 mg/mL Van hydrochloride (Aladdin, China) 2 mg/mL, 20 mM 2-Piperidineethanol, and incubated at 37 °C for 24 h. Another deposition of 24 h for scaffolds was adopted in the refreshed deposition solution. Then, samples were ultrasonically cleaned to remove the loosely adhered PDA deposits and dried in vacuum. The coated samples were recorded as PV/Zn–1Mg. CaP solution was prepared to deposit HA coating on PDA coating [52]. The composition of CaP solution was as follows: 7 mM $Ca(NO_3)_2{\cdot}4H_2O$, 4.2 mM $NaH_2PO_4{\cdot}2H_2O$, and 2 mM $NaHCO_3$. The PV/Zn–1Mg samples were immersed in the CaP solution at 37 °C for 12 h. After refreshing CaP solution, the deposition lasted for another 12 h. Samples were dried in an oven at 37 °C. Then, the BMP2 solution, with the solvent composition of 15 mM Tris, 0.5 M Urea, 25 mM Ches, 5% DMF, was diluted with phosphate-buffered saline (PBS) to 10 μg/mL. The above samples were incubated aseptically in 2 mL BMP2 solution at 4 °C for 24 h, and dried on the ultra-clean bench. The samples were recorded as HB/PV/Zn–1Mg. The preparation process and overview pictures of samples were shown in Fig. 1b and c.

2.2. Coating characterization

The morphology and element distribution of coatings were observed by SEM and EDS. An X-ray diffractometry (XRD, Rigaku SmartLab 9 kW, Japan) and attenuated total reflection-Fourier transform infrared spectroscopy (ATR-FTIR, Thermo Scientific Nicolet iS20, USA) were utilized to identify the composition of coatings. The static water contact angle of bulk samples was measured by a contact angle meter (Kino SL150E, USA). To visualize BMP2 on samples, FITC conjugation kit (Sangon

biotech, China) was utilized. The FITC-labeled BMP2 was immobilized on the HA coated samples, and then BMP2 was visualized as fluorescent signals by fluorescence microscope imaging (Olympus, Japan). For identifying the release behavior of BMP2, HB/PV/Zn–1Mg scaffolds were incubated in 5 mL PBS solution at 37 °C in a 5% CO_2 incubator for 21 days. At day 1, 3, 5, 7, 14, and 21, 1 mL immersion solution was taken out for analysis and replaced with the same amount of fresh PBS solution. The enzyme-linked immunosorbent assay kits (ELISA, Abcam, UK) were used for BMP2 quantification. As for the detection of the release of Van, samples loaded with Van were immersed in 20 mL PBS solution, and incubated in a shaking incubator (80 rpm, 37 °C). At specific time points (30 min, 1 h, 2 h, 4 h, 8 h, 16 h, 32 h, 3 d, 6 d, 12 d, 24 d), 1 mL immersion solution was taken out for analysis and replaced with the same amount of fresh PBS solution. The concentration of Van in the PBS solution was detected by UV/vis spectrophotometer (Ultrospec 1100 pro, USA) at the wavelength of 236 nm.

2.3. In vitro degradation tests

Immersion tests were performed in 40 mL m-SBF solution at 37 °C for 28 days. The m-SBF solution was refreshed every 2 days. After immersion, samples were rinsed using distilled water and dried in an oven at 37 °C, and then weighted. The characterization of surface morphology and composition was conducted by SEM and EDS. The concentration of Zn^{2+} was detected by inductively coupled plasma-mass spectrometry (ICP-MS, Agilent 7700, USA). The electrochemical tests were conducted with an electrochemical workstation (Autolab, Metrohm, Switzerland) at 37 °C in the modified simulated body fluid (m-SBF, Table S1). A standard three-electrode system was utilized with the sample as the working electrode, a platinum plate as the counter electrode and a saturated calomel electrode as the reference electrode. The tests were composed of open circuit potential (OCP) measurements, electrochemical impedance spectroscopy (EIS) scan and potentiodynamic polarization (PDP) tests. The OCP tests were carried out with a time period of 3600 s. After OCP, EIS measurements were performed over a frequency range of 10^{-2}–10^{-5} Hz with a perturbation of 10 mV. The equivalent circuits were obtained by NOVA 1.11 software (Autolab, Metrohm, Switzerland). PDP scan was performed at a scan rate of 1 mV/s. The corrosion potential (E_{corr}) and corrosion current density (i_{corr}) were analyzed by Tafel extrapolation and linear fit. An average of three samples were taken for each group. Furthermore, the corrosion rate (CR) was calculated according to formula 1, where i_{corr} was corrosion current density (μA/cm^2), EW represented equivalent metal weight, and ρ was density. For Zn–1Mg, as reported in the literature, EW was 32.15, and ρ was 7.09 g/cm^3 [53].

$$CR = 3.27 \times 10^{-3} \frac{i_{corr} EW}{\rho} \quad (1)$$

2.4. In vitro biocompatibility and anti-bacterial activity

2.4.1. Cell viability tests

Mouse osteoblast precursor cells (MC3T3-E1) were purchased from the Cell Bank of the Chinese Academy of Sciences (Shanghai, China). MC3T3-E1 cells were cultured at 37 °C, 5% CO_2 and 95% humidified atmosphere using α-MEM (Gibco, USA) complete medium containing 10% fetal bovine serum (FBS, Gibco, USA) and 1% penicillin-streptomycin solution (Solarbio, China), and sub-cultured when cells reached 80%–90% confluence. Cells in passages 3–8 were used in this study. The extracts of samples were obtained according to ISO 10993–5. All samples were sterilized by Co-60 irradiation. Subsequently, samples were immersed in α-MEM complete medium for 24 ± 0.5 h at 37 °C in a cell incubator, with an extraction ratio of 1.25 cm^2/mL. Given the slow degradation rate of Zn-based BMs *in vivo*, and the rapid metabolic exchange of corrosion products, 1-fold and 2-fold diluted extracts were used for subsequent *in vitro* experiments [34]. The Cell Counting Kit-8 (CCK-8, APExBIO, USA) was used to evaluate the cell viability of MC3T3-E1. The cells were seeded into a 96-well plate at a density of 2 × 10^3/well until cells attached to the well bottom. Then, the original medium was replaced by extracts to continue the culturing for 1, 3 and 5 days. At specific time points, 10 μL CCK-8 solution was added at 37 °C for 1 h in the dark. The optical density (OD) value was detected at 450 nm using a microplate reader (Bio-Tek, USA). As for Live/dead staining, MC3T3-E1 cells were co-cultured with extracts. The cells were stained with a Live/Dead cell staining kit (Beyotime, China) and observed by a fluorescence microscope to assess survival and morphology of cells.

2.4.2. In vitro osteogenic differentiation

MC3T3-E1 cells were seeded in a 12-well plate at a density of 2 × 10^4/mL, and cultured with osteogenic induction extracts, which contained sample extracts, 10 mM β-glycerophosphate (Sigma, USA), 0.1 mM dexamethasone (Solarbio, China) and 50 μg/mL vitamin C (Solarbio, China). After 7 days of incubation, cells were lysed using inhibitor-free Western and IP cell lysates (Beyotime, China) and total protein was extracted. The bicinchoninic acid protein assay kit (BCA, Thermo Fisher, USA) was used to determine the total protein content. The ALP detection kit (Beyotime, China) was applied to detect the ALP activity of MC3T3-E1. The results were expressed in U per mg of total protein. Moreover, MC3T3-E1 cells were stained using an ALP staining kit to evaluate the formation of calcified nodules. Alizarin red (Solarbio, China) was used to stain MC3T3-E1 after 21 days of culturing. Then, mineralized nodules were dissolved using 10% of cetylpyridinium chloride (Solarbio, China) and measured the absorbance at 562 nm.

2.4.3. Osteogenesis-related protein and gene expression

The Western blot was used to evaluate the osteogenesis-related protein expression. MC3T3-E1 cells were cultured in the osteogenic induction extracts for 7 days, and the cultured cells were lysed by RIPA buffer (Thermo Fisher, USA). The protein concentration was determined and normalized by BCA kit. Protein samples were heated at 98 °C for 5 min, and were loaded into SDS-PAGE and transferred to a polyvinylidene fluoride (PVDF) membrane. Then, the PVDF membrane was incubated in a blocking solution (5% BSA) for 2 h. After cleaning, the PVDF membrane was incubated overnight in the Runx2 and ostopontin (OPN) antibody solution at 4 °C. Subsequently, PVDF membranes were incubated with secondary antibody for 2 h. The reaction was performed with a chemiluminescent reagent, and the PVDF membrane was exposed and imaged. The Western blot images were semi-quantitatively analyzed by Image J software.

The expression of osteogenesis-related genes was detected by a real-time polymerase chain reaction (RT-PCR). The MC3T3-E1 cells were seeded in a six-well plate and cultured for 7 days with osteogenic induction extracts. The total RNA was extracted using the Trizol reagent (Ambion, USA). Then, the RNA was reversed and transcribed into complementary DNA using the Prime Script™ RT reagent kit (Vazyme, USA). The corresponding forward and reverse primers were shown in Table S2 β-actin was selected as the internal reference to detect the expression levels of osteogenesis-related genes. Real-time fluorescence quantitative PCR instrument (Quant Studio 5, Applied biosystems, USA) was used to perform real-time PCR assays. QuantStudio™ design & analysis software v1.4 was utilized for data analysis.

2.4.4. In vitro antibacterial activity

Staphylococcus aureus (*S.aureus*, ATCC 25923) and escherichia coli (*E.coli*, ATCC 25922) purchased from Beijing Microbiological Culture Collection Center were used to evaluate the *in vitro* antibacterial activity. Bacteria were incubated in tryptone soy broth (TSB, Solarbio, China), and centrifuged, collected, and adjusted to a concentration of 1 × 10^6 CFU/mL for further use. Samples were placed in 5 mL bacterial suspension with a concentration of 1 × 10^6 CFU/mL, and incubated for 24 h at 37 °C. Then, the bacterial suspension was serially diluted to spread evenly onto the tryptone soy agar (TSA, Solarbio, China) bacterial

culture plates, and incubated at 37 °C for 24 h. The number of colonies formed on the plate was counted to evaluate the antibacterial activity. Samples co-cultivated with the bacterial suspension for 24 h were washed with PBS. The bacteria adhered to samples were fixed with 4% paraformaldehyde, then dehydrated by ethanol (30%, 50%, 70%, 80%, 90%, 95%, 100%, 100%) gradient dehydration, and dried in a vacuum drying oven. The bacterial morphology was observed using SEM.

2.5. In vivo tests

2.5.1. Surgical procedure

The porous cylindrical samples (Φ 2.55 mm × 5.7 mm) were used for *in vivo* implantation. All animal operations were approved by the Animal Ethics Committee of the Beijing Keyu Animal Breeding Center (KYLL0001089). 24 male rats with a weight of 200–250 g were anesthetized with an intraperitoneal injection of ketamine (10 mg/kg, Dr. Ehrenstorfer GmbH, Germany) and 2% xylazine (10 mg/kg, Fluorochem, UK). A longitudinal incision was made lateral to the patellar ligament to expose the lateral femoral condyle. A bicortical perforating bone defect model for rat lateral femoral condyle was established via drilling with a 3 mm drill bit. Samples were implanted into the defect, and the surgery site was sutured layer by layer. The rats were euthanized after 4, 8, and 12 weeks of implantation to collect femurs.

2.5.2. Micro-computed tomography (Micro-CT) analysis

The femurs of the rats were collected and fixed with a 10% neutral formaldehyde fixative. The femur specimens were scanned by a Micro-CT scanner (Zeiss Xradia 520 Versa, Germany, 120 kV, 66.7 μA). Then, the three-dimensional (3D) imaging was reconstructed by the 3D image processing software CTvox 3.0 (Bruker, Germany), and a 0.5 mm diameter area around the implant was set as the region of interest (ROI) using CT Analyser 1.15.2.2 software (Bruker, Germany). Histomorphometric indexes, including bone volume fraction (BV/TV), trabecular numbers (Tb.N), trabecular separation (Tb.Sp), and trabecular thickness (Tb.Th), were quantitatively analyzed in ROIs.

2.5.3. Histological evaluation

Hard-tissue slicing and staining were conducted on the rat femur. The femur specimens were rinsed in water, dehydrated in ethanol, and then cleaned in xylene. Finally, samples were embedded in methyl methacrylate. Each sample was cut along the horizontal plane of the femur (parallel to the implant) to obtain 3–4 200 μm-thick slices. Subsequently, the slice of femurs was further ground to 100 μm-thick. Methylene blue-fuchsin basic staining was performed, and slices were imaged using a high-resolution microscope. As for the evaluation of biosafety, the vital organ (heart, liver, spleen, lung and kidney) specimens of rats were collected at week 12 after implantation. All collected organs were fixed in 10% neutral formaldehyde fixative, and then dehydrated, embedded, and stained using hematoxylin-eosin (H&E) to observe possible pathological changes.

2.5.4. In vivo antibacterial activity

After constructing a bicortical perforating bone defect of femoral condyles in SD rats, 10 μL *S. aureus* bacterial suspension (1×10^7 CFU/mL) was inoculated into the bone defect. Then, samples were implanted into the infected bone defect. The rats were euthanized at day 7 after surgery, and the femur specimens were collected. Ultrasonication was used to separate the bacteria in the bone tissue and surface of the implants respectively, and the bacteria were cultured on the TSA bacterial culture plates for 24 h and counted to assess the *in vivo* antibacterial activity. In addition, the femur without implants were fixed in 10% neutral formaldehyde fixative, decalcified in 10% EDTA for 6 weeks, dehydrated through an ethanol gradient, embedded in paraffin and sliced along the horizontal plane of the implant. Finally, the H&E staining was performed, and slices were imaged using a high-resolution microscope.

2.6. Statistical analysis

All quantitative data were expressed as Mean ± standard deviation (SD). The SPSS 23.0 statistical software (IBM, USA) was used to assess the statistical significance of the data by the one-way analysis of variance (ANOVA). $^*p < 0.05$ or $^{**}p < 0.01$ were considered statistically significant.

3. Results

3.1. Coating characterization

As shown in Fig. 2a, after the NaOH heat treatment, a layer composed of fine hexagonal crystal, which was similar to the hexagonal wurtzite structure of ZnO, appeared on the surface of activated Zn–1Mg scaffold with a thickness around 45 μm (Fig. 2b). The EDS results (Table 1) indicated that the content of O on the surface of activated Zn–1Mg scaffold was higher compared to that of Zn–1Mg. After PDA coating immobilization, PV/Zn–1Mg scaffolds showed a typical black appearance, as shown in Fig. 1c. In SEM images of surface and cross-section, numerous PDA microspheres were observed to adhere uniformly and densely along the hexagonal crystals on the surface of scaffolds. The presence of N and Cl element indicated that PDA coating loaded with Van was successfully immobilized on scaffolds. Furthermore, after the modification of HA coating, HB/PV/Zn–1Mg scaffolds showed a grayish-black appearance. The typical HA petal-like crystals were observed adhering to the surface of PDA microspheres. The presence of Ca and P also indicated the successful preparation of HA coating.

The XRD pattern was shown in Fig. 2c. Powder diffraction file (PDF) cards were used to detect phases. Strong diffraction peaks corresponding to Zn (PDF 65–3358) were identified in Zn–1Mg scaffolds. Moreover, diffraction peaks of secondary phases including $MgZn_2$ (PDF 65–2226) and Mg_2Zn_{11} (PDF 65–1853) were also found. ZnO (PDF 36–1451) peaks were detected in activated Zn–1Mg, PV/Zn–1Mg and HB/PV/Zn–1Mg. However, $MgZn_2$ and Mg_2Zn_{11} peaks were scarcely observed in these samples, indicating that Zn oxides covered the surface of Zn–1Mg samples. In addition, no diffraction peak of HA was found in XRD profiles of HB/PV/Zn–1Mg, mainly attributed to the low HA content. Fig. 2d showed the ATR-FTIR spectra of samples. In activated Zn–1Mg and PV/Zn–1Mg scaffolds, the absorption peak at 620 cm^{-1} was corresponding to the existence of ZnO, confirming that NaOH heat treatment produced a large number of oxides on the surface of Zn–1Mg. For PV/Zn–1Mg and HB/PV/Zn–1Mg samples, the characteristic peak of 3255 cm^{-1} was attributed to the O–H and N–H stretching vibration. Moreover, the recognition of C═C and C═N bonds at 1640 cm^{-1} and 1476 cm^{-1} proved the existence of PDA. For HB/PV/Zn–1Mg scaffolds, absorption peaks at 1022 cm^{-1}, 600 cm^{-1} and 558 cm^{-1} corresponded to PO_4^{3-} characteristic bands, and the sharp splitting of the P–O bond indicated the existence of crystal structure of apatite. Characteristic bands of CO_3^{2-} appeared in 822 cm^{-1}, 1350 cm^{-1} and 1420 cm^{-1}, indicating the obtained HA had low crystallinity and contained trace carbonate, similar to the composition of natural bone apatite.

As shown in Fig. S1, numerous BMP2 molecules with green fluorescence signal were observed on the surface of HB/PV/Zn–1Mg, with strong and uniform fluorescence signal, which indicated that plenty of BMP2 was uniformly loaded. The release profile of BMP2 was detected by ELISA (Fig. 2e). An initial burst release of BMP2 was observed. The released BMP2 in day 1 accounted for almost 60% of the total release in 21 days. Subsequently, BMP2 released slowly in day 2–14. In day 14–21, the release rate of BMP2 suddenly increased, attributed to the peeling of the coating. As for Van, the release profiles were shown in Fig. 2f and g. A burst release was also found in the first few hours. The amount of Van released in first 16 h was about 40–50% of the total release in 24 days, and then slowly increased to 56–70% in the following 6 days. It was worth noting that the rapid release of Van was observed in day 6–12, indicating an earlier coating peeling, attributed to the fact that the test of

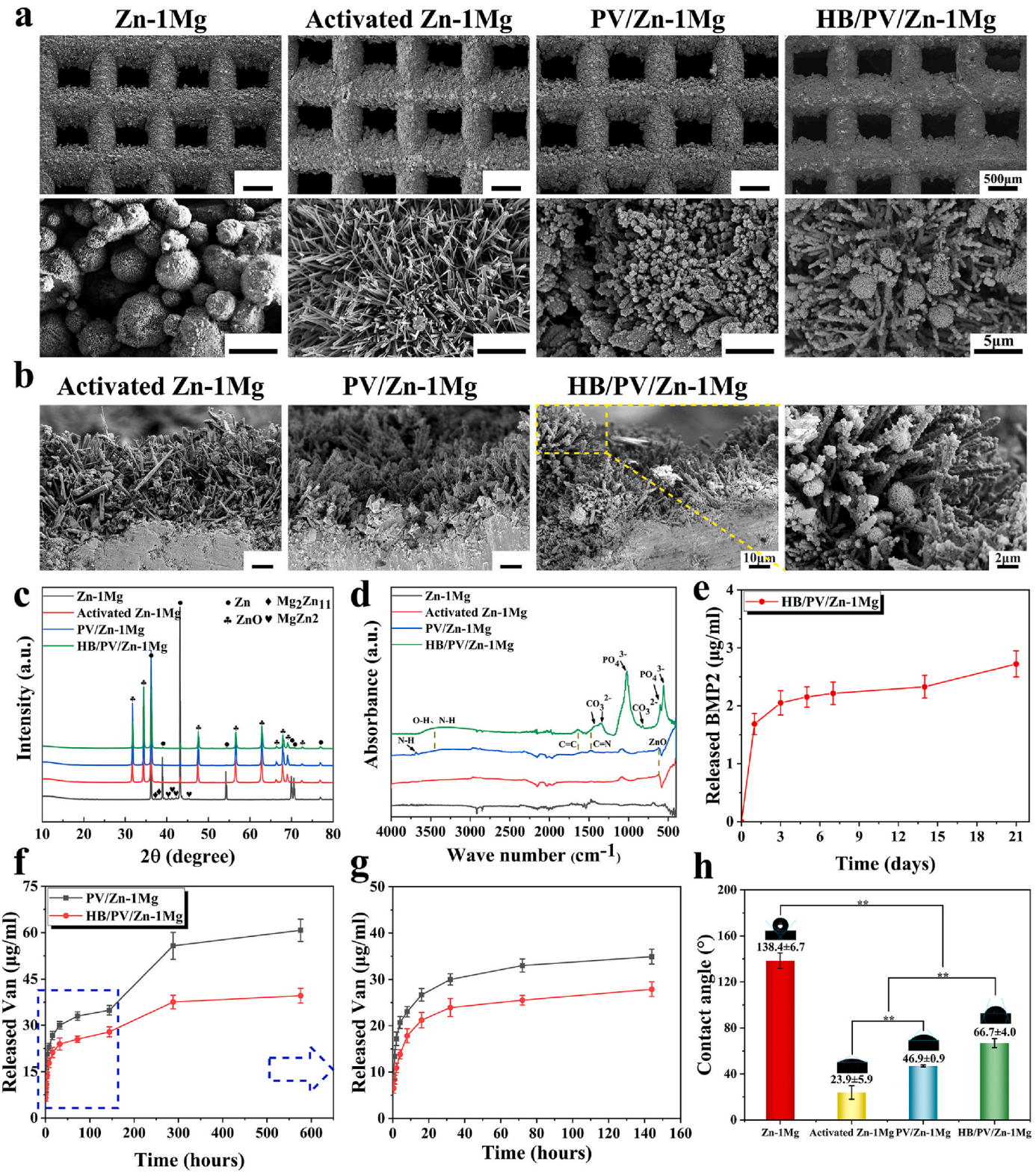

Fig. 2. Coating characterization: Morphology of surface (a) and cross section (b) of coatings; (c) XRD pattern; (d) ATR-FTIR spectra; Release profile of BMP2 (e) and Van (f ~ g); (h) Static water contact angle evaluation.

Van was performed under shaking. After day 12, the release of Van was continued at a slow rate. During the test, the cumulative release of Van of HB/PV/Zn–1Mg was significantly lower than that of PV/Zn–1Mg, resulted from the loss of Van during the preparation of HA coating.

Fig. 2h showed that the static water contact angle of different samples. The wetting angle of Zn–1Mg scaffold was 138.4 ± 6.7°, showing a hydrophobic state. After the NaOH heat treatment, the contact angle of the activated Zn–1Mg decreased to 23.9 ± 5.9°, suggesting ZnO passivation layer greatly improved the surface hydrophilicity. With the adhesion of PDA coating, the contact angle of PV/Zn–1Mg increased to 46.9 ± 0.9°. After further immobilizing the HA coating on the surface of the PDA coating, the contact angle of the HB/PV/Zn–1Mg increased to

Table 1
Element compositions (in wt.%) of Zn–1Mg, Activated Zn–1Mg, PV/Zn–1Mg and HB/PV/Zn–1Mg.

Samples	Elements							
	C	N	O	Zn	Mg	Cl	Ca	P
Zn–1Mg	1.93	/	2.58	94.21	1.28	/	/	/
Activated Zn–1Mg	9.70	/	21.56	67.30	1.44	/	/	/
PV/Zn–1Mg	11.61	2.84	13.20	71.27	0.60	0.48	/	/
HB/PV/Zn–1Mg	4.47	2.73	28.33	45.23	0.32	0.37	8.92	9.64

66.7 ± 4.0°.

3.2. *In vitro* degradation behavior

The results of electrochemical tests were shown in Table S4. As shown in Fig. S2a, compared with −1.150 V_{SCE} of Zn–1Mg, PV/Zn–1Mg and HB/PV/Zn–1Mg showed higher OCP values, −0.934 and −0.830 V_{SCE} respectively, indicating higher corrosion resistance. The results of EIS measurements were presented in Fig. S2b. Three equivalent circuit models, as shown in Fig. S3c were utilized for the fitting of EIS, and the fitting results were listed in Table S3. R_s represented the resistance of m-SBF solution. R_1 and CPE_1 referred to the charge transfer resistance and double-layer capacity. R_2, R_3 and CPE_2, CPE_3 were applied for descripting capacitance and resistance of coatings. The total resistance R_p could be obtained by summing up R_1, R_2, and R_3. The R_p value of Zn–1Mg, PV/Zn–1Mg and HB/PV/Zn–1Mg samples was 245, 7619 and 37068 Ω cm^2, proving the greatly increased corrosion resistance resulted from coating. PDP curves were shown in Fig. 3c, and the data calculated by Tafel fitting were provided in Table S4. The corrosion rates (*CR*) were ranked in a descending order: Zn–1Mg > PV/Zn–1Mg > HB/PV/Zn–1Mg, indicating the improved corrosion resistance of samples with coating, which was in line with OCP and EIS analysis. Therefore, as discussed above, coatings greatly decreased the corrosion rate of Zn–1Mg scaffolds, which may be attributed to the physical barrier effect

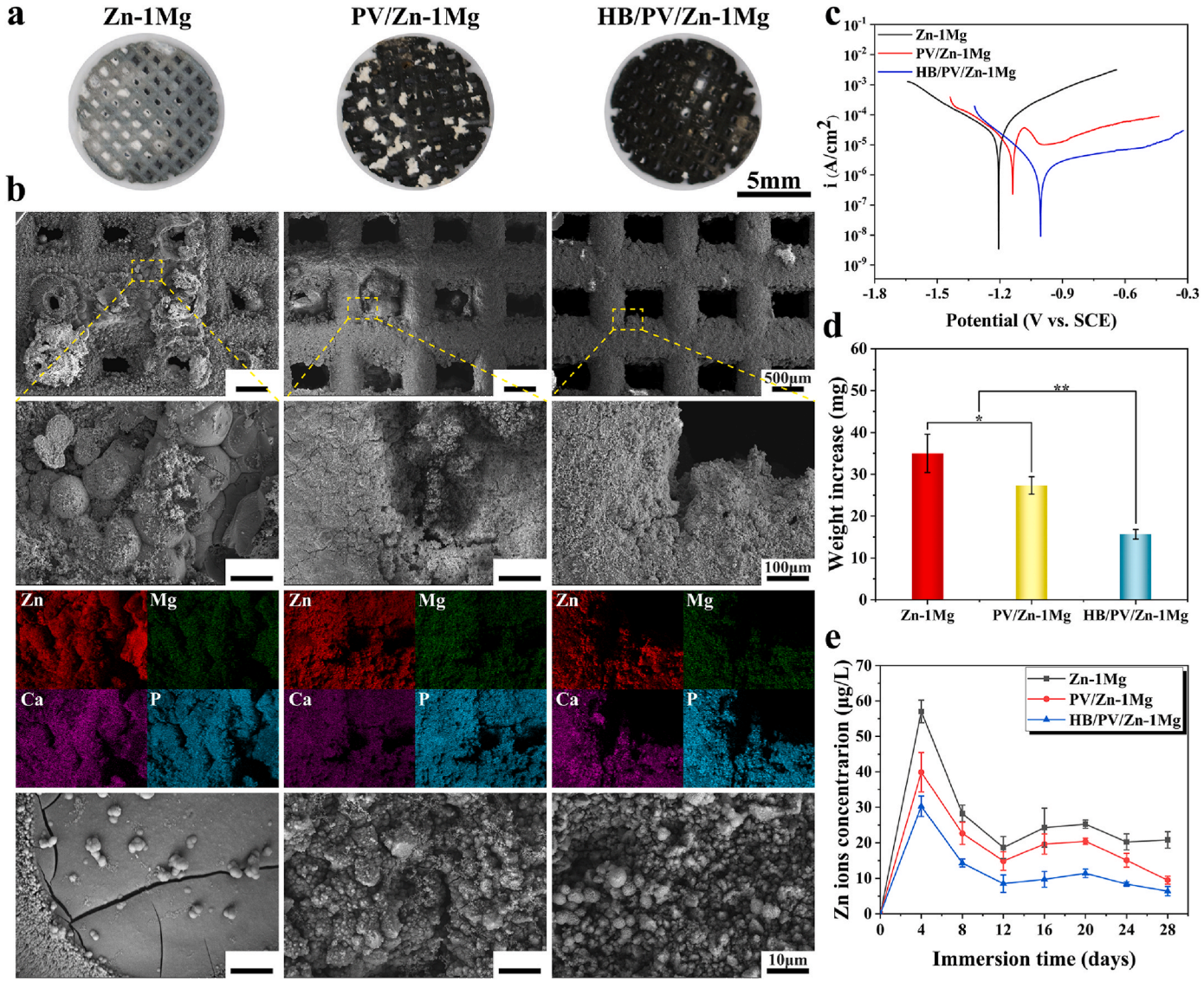

Fig. 3. *In vitro* degradation behavior: (a) Overview pictures and (b) SEM and EDS scan of samples after 28-days immersion in m-SBF; (c) PDP curves; (d) Weight increase after immersion, and (e) Zn^{2+} concentration in m-SBF.

of HA and PDA coatings on corrosive medium. And compared with the single-layer PDA coating, the HA/PDA composite coating had a more significant effect on improving the corrosion resistance.

In vitro degradation behavior was further evaluated by immersion tests. As shown in Fig. 3a, compared with Zn–1Mg and PV/Zn–1Mg, fewer corrosion products were observed in HB/PV/Zn–1Mg scaffold. According to Fig. 3b, a large amount of corrosion products blocked the pores in Zn–1Mg group, and some corrosion products were also observed in the pores of the PV/Zn–1Mg. However, no obvious corrosion products were observed in the pores of HB/PV/Zn–1Mg. In the enlarged SEM image, spherical corrosion products were observed at the surface of Zn–1Mg. For PV/Zn–1Mg and HB/PV/Zn–1Mg, corrosion products were evenly distributed on the coating surface, and the amount of corrosion products was significantly higher in PV/Zn–1Mg. Moreover, a clear enrichment of Zn, Mg, Ca and P was found at the surface of samples in EDS results, implying the presence of calciate, phosphates and oxides of Zn or Mg in corrosion products. The amount of corrosion products was closely related to the degradation rate of scaffolds. The weight increase of samples after the immersion was shown in Fig. 3d. The weight increases of PV/Zn–1Mg and HB/PV/Zn–1Mg was significantly lower than that of the Zn–1Mg, which could be explained by the higher degradation rate of Zn–1Mg, thus resulting in more accumulation of corrosion products. The concentration of Zn^{2+} in the immersion solution was shown in Fig. 3e. In the initial 4 days, the release of Zn^{2+} in all samples was rapid. During day 8–28, the release of Zn^{2+} gradually tended to be stable. The PV/Zn–1Mg and HB/PV/Zn–1Mg showed significantly lower Zn^{2+} content at all time than that of Zn–1Mg, and the HB/PV/Zn–1Mg had the lowest Zn^{2+} concentration. The results of immersion test were consistent with electrochemical results.

3.3. *In vitro* biocompatibility and antibacterial activity

3.3.1. *Cell viability*

MC3T3-E1 cell viability was examined using the CCK-8 method (Fig. 4a and b). The 1-fold diluted extracts of Zn–1Mg and PV/Zn–1Mg groups exhibited significant cytotoxicity, and the cell viability decreased with the extension of culture time. By comparison, the cell viability of the HB/PV/Zn–1Mg group could reach 120–150% in 1-fold diluted extracts. For the 2-fold diluted extracts, all sample groups showed improved cytocompatibility. Among them, HB/PV/Zn–1Mg group showed the highest cell viability. Fig. 4c showed Zn^{2+} and Mg^{2+} concentration in extracts. HB/PV/Zn–1Mg group had significantly lower Zn^{2+} and Mg^{2+} concentration. There was no significant difference in the Zn^{2+} concentration between PV/Zn–1Mg and Zn–1Mg groups, but the Mg^{2+} concentration was significantly lower in the PV/Zn–1Mg group. The cell viability was further analyzed using Live/dead staining (Fig. 4d). For 1-fold diluted extracts, Zn–1Mg and PV/Zn–1Mg groups had sparse green fluorescence in comparison with the negative control group, and an obvious red fluorescence, representing dead cells, was observed in Zn–1Mg group. In enlarged images, the morphology of all cells had a rounded phenotype in Zn–1Mg and PV/Zn–1Mg groups. While, a large number of viable cells were found in HB/PV/Zn–1Mg group, and exhibited better spreading morphology. For 2-fold diluted extracts, the number and morphology of viable cells were similar to those of negative control group in all sample groups, which was consistent with the CCK-8 results.

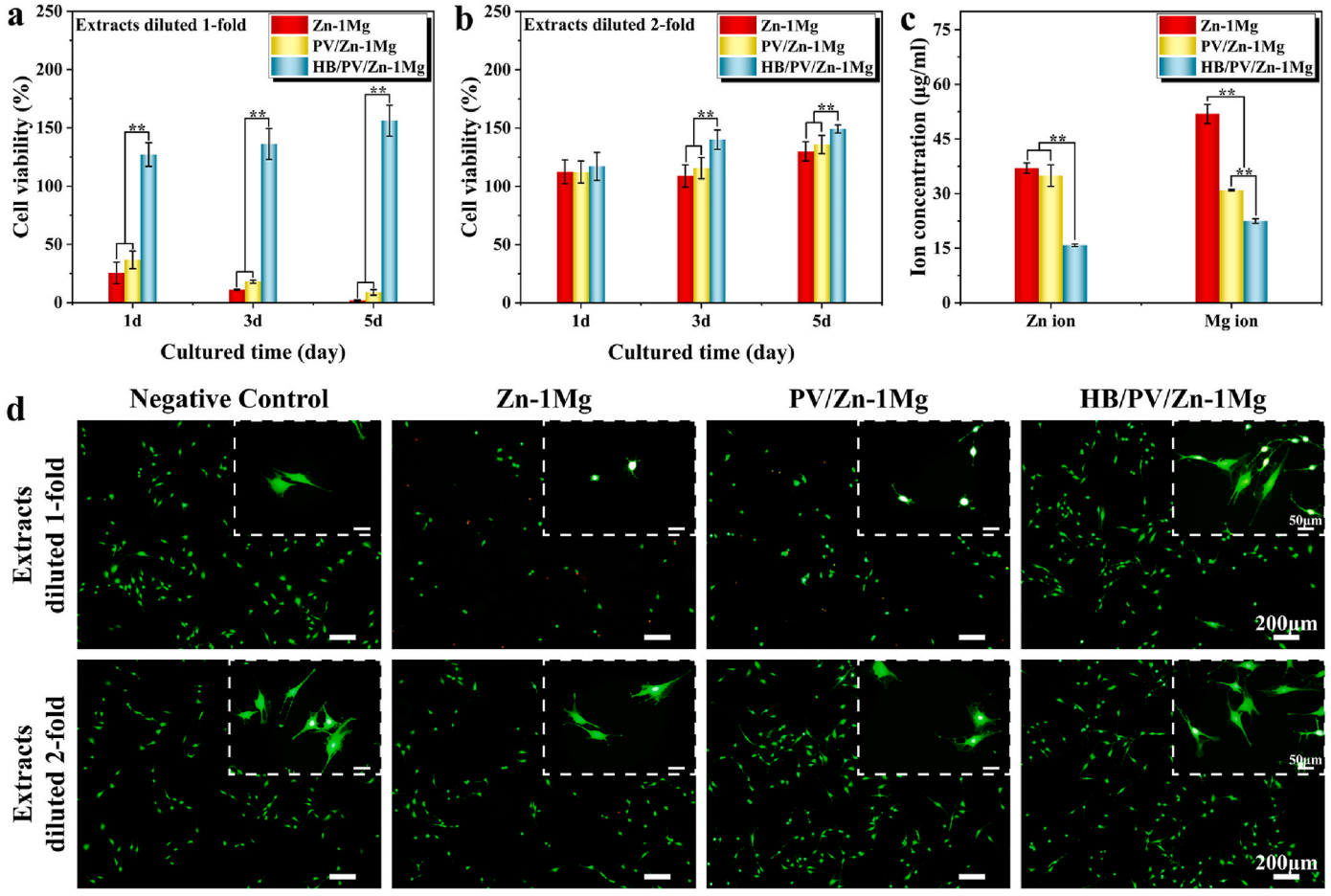

Fig. 4. The viability of MC3T3-E1 cells co-cultured with different sample extracts: (a) Extracts diluted 1-fold, (b) Extracts diluted 2-fold; (c) Concentration of Zn^{2+} and Mg^{2+} in the extracts; (d) Images of live/dead cell staining.

3.3.2. In vitro osteogenic differentiation

ALP and Alizarin Red staining were performed to detect the osteogenic differentiation and mineralization of MC3T3-E1 cells. As shown in Fig. 5a, cells in Zn–1Mg and PV/Zn–1Mg groups almost died in 1-fold diluted extracts. However, HB/PV/Zn–1Mg group showed higher ALP activity than that of negative control group and enhanced extracellular matrix mineralization. For 2-fold diluted extracts, the osteogenic differentiation and mineralization levels ranked as HB/PV/Zn–1Mg > PV/Zn–1Mg and Zn–1Mg > negative control. Furthermore, the quantitative and semi-quantitative analysis of ALP activity and mineralization levels verified these observations (Fig. 5b and c). The expression levels of osteogenic markers (Runx2 and OPN) were detected to further analyze the osteogenic differentiation potential. The expression levels of the osteogenic markers were markedly up-regulated in all sample groups, as indicated by Western blot analysis (Fig. 5d and e). The Runx2 and OPN expression levels of the HB/PV/Zn–1Mg group were significantly higher than Zn–1Mg and PV/Zn–1Mg groups. RT-PCR results (Fig. 5f) exhibited a similar trend as indicated by Western blot.

3.3.3. In vitro antibacterial activity

Antibacterial activity was assessed using the spread plate method (Fig. 6a and b). The Zn–1Mg group showed slight antibacterial activity. In contrast, the bacteriostatic efficacy of PV/Zn–1Mg and HB/PV/Zn–1Mg groups was significantly stronger than that of Zn–1Mg group. Notably no bacterial colonies were visible in the PV/Zn–1Mg group. In addition, the adhesion morphology of *E. coli* and *S. aureus* was also observed (Fig. 6c). A large number of bacteria was observed on the surface of Zn–1Mg scaffolds. In contrast, limited amounts of bacteria adhered to the surface of PV/Zn–1Mg and HB/PV/Zn–1Mg scaffolds. More importantly, *E. coli* and *S. aureus* on the surface of PV/Zn–1Mg and HB/PV/Zn–1Mg scaffolds exhibited morphologies of distortion, shrinkage and even dissolution. Only a little amount of *E. coli* cell wall ruptures were observed on the surface of Zn–1Mg scaffolds.

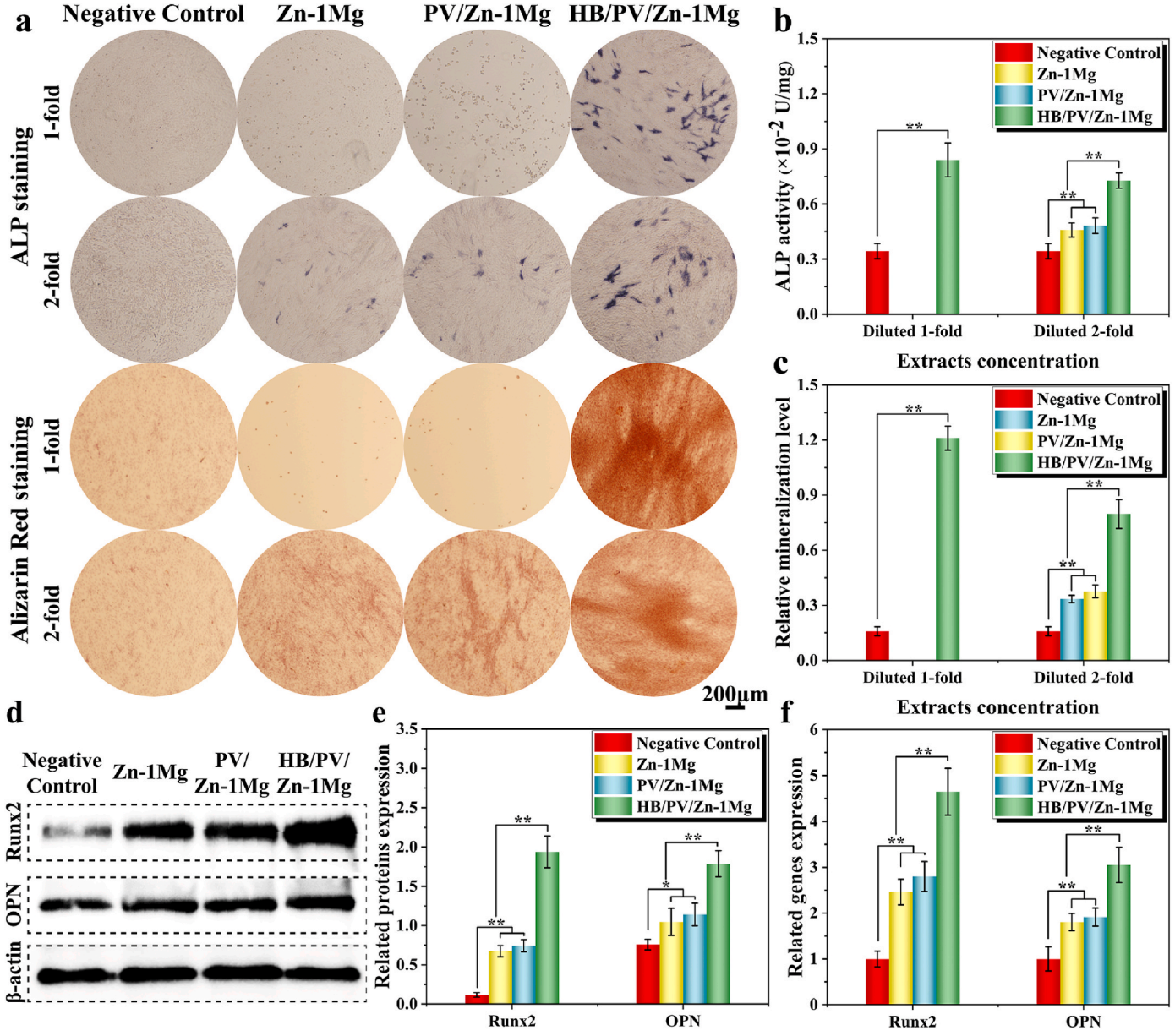

Fig. 5. In vitro osteogenic differentiation: (a) ALP and Alizarin Red staining; (b, c) Quantitative and semi-quantitative analysis of ALP activity and mineralization levels; Expression level of osteogenesis-related (d, e) proteins and (f) genes.

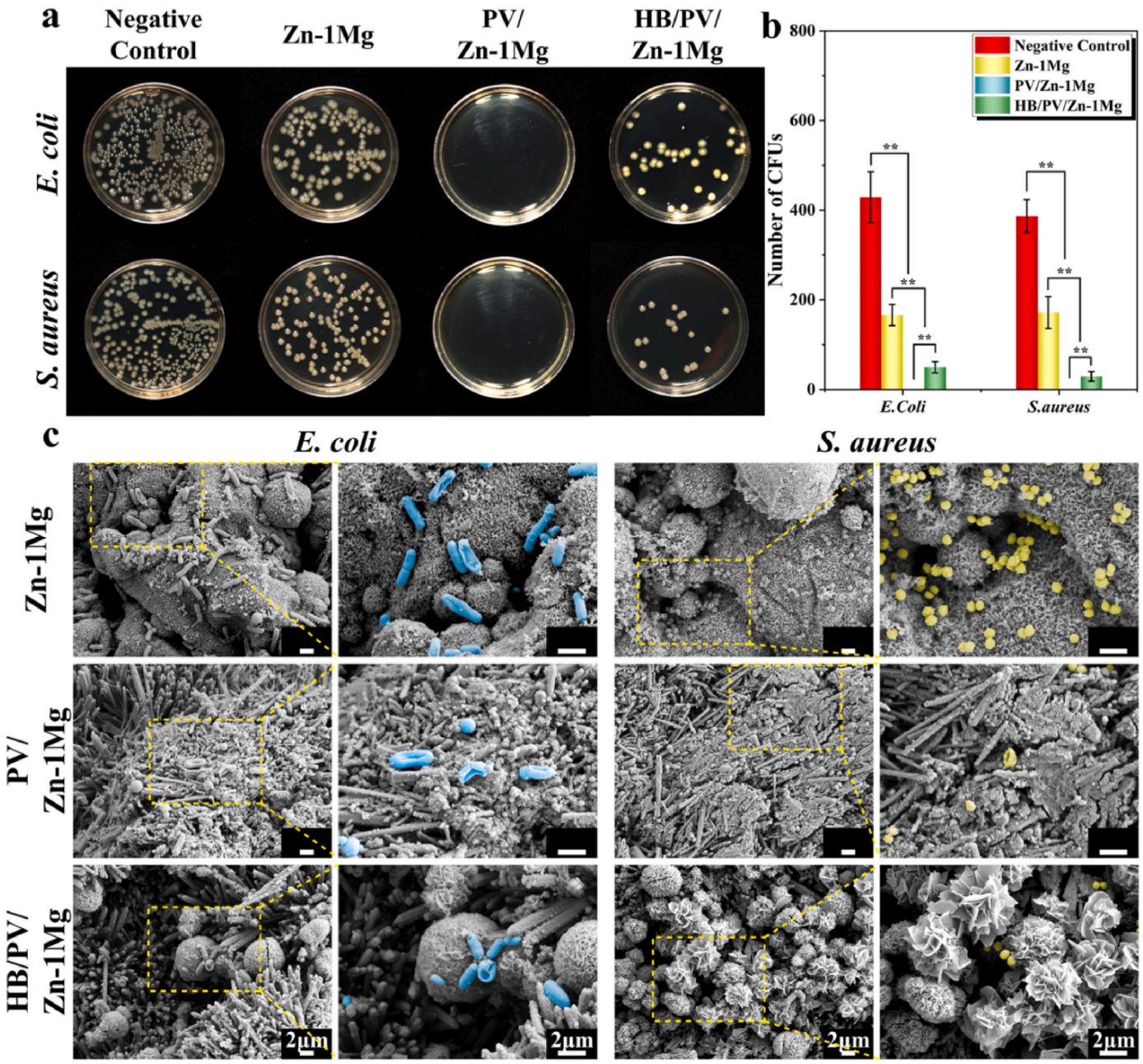

Fig. 6. Antibacterial activity *in vitro*: (a) Images of *E. coli* and *S. aureus* bacterial colonies after co-cultured with samples; (b) The relative bacterial viability; (c) SEM images of *E. coli* and *S. aureus* morphology.

3.4. In vivo animal experiments

3.4.1. Micro-CT analysis

As shown in Fig. 7a, a small amount of new bone formation was observed around all scaffolds at week 4 after surgery. After 8 weeks of the implantation, the new bone around PV/Zn–1Mg and HB/PV/Zn–1Mg scaffolds was significantly more than that of Zn–1Mg scaffold. HB/PV/Zn–1Mg showed a better healing status than PV/Zn–1Mg group. The amount of new bone increased gradually with time passing by. At week 12 after implantation, the amount of new bone tissue was highest in HB/PV/Zn–1Mg, followed by PV/Zn–1Mg group. In addition, the quantitative analysis results in Fig. 7b verified the favorable osteogenic activity of HB/PV/Zn–1Mg *in vivo*. Four osteogenic indices obtained from Micro-CT, including BV/TV, Tb. N, Tb. Th and Tb. Sp, exhibited significant differences between Zn–1Mg and HB/PV/Zn–1Mg group. The higher BV/TV, Tb. N, Tb. Th and lower Tb. Sp were found in the HB/PV/Zn–1Mg group.

3.4.2. Histological evaluation

Hard tissue sections were shown in Fig. 8, where red areas indicated regenerated bone. The full-view images of the sections confirmed that mass of regenerative bone increased over time in all sample groups, and it was the highest in HB/PV/Zn–1Mg, followed by PV/Zn–1Mg. Many biodegradable products were observed in the Zn–1Mg scaffold. While, only a little amount of degradation products was observed in PV/Zn–1Mg at week 12, and no obvious degradation products were observed in HB/PV/Zn–1Mg. Overall, the HB/PV/Zn–1Mg scaffold exhibited the slowest degradation rate *in vivo*. For enlarged images, compared with Zn–1Mg scaffolds, better osseointegration and favorable bone ingrowth were observed in PV/Zn–1Mg and HB/PV/Zn–1Mg, and significantly more new bone formation was observed in HB/PV/Zn–1Mg. These observations were consistent with the Micro-CT results.

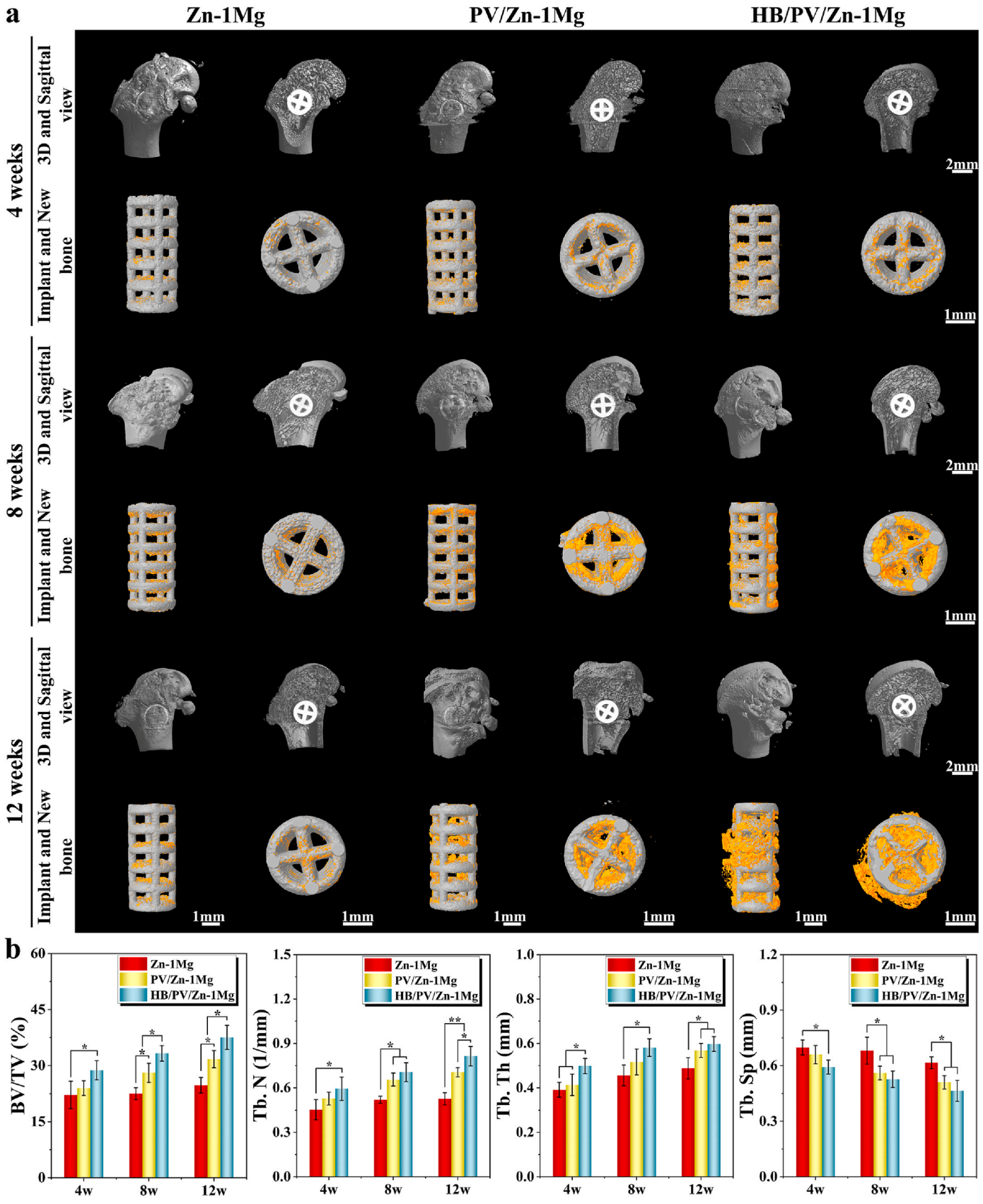

Fig. 7. (a) Micro-CT images at 4, 8, and 12 weeks of *in vivo* implantation including new bone and implants images; (b) Quantitative analysis of osteogenic ability.

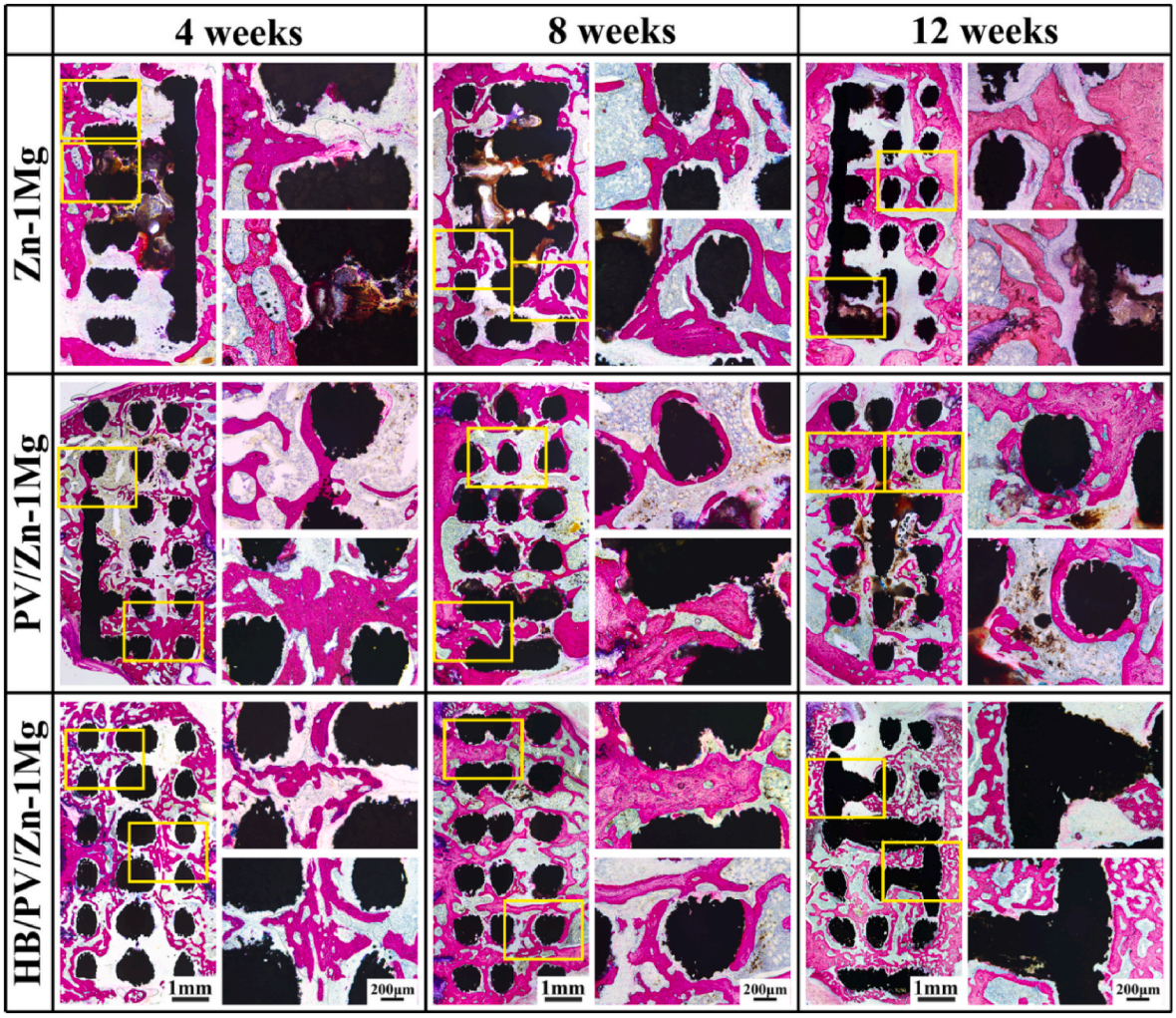

Fig. 8. Full-view and enlarged images of hard-tissue slices of Zn–1Mg, PV/Zn–1Mg and HB/PV/Zn–1Mg implanted *in vivo*.

The H&E staining results of rat vital organ including heart, liver, spleen, lung, and kidney sections were shown in Fig. S3. No abnormalities or pathological morphologies were observed in all tissue sections, indicating no abnormality in vital organ function in experimental animals, and revealing all scaffolds had a good *in vivo* biosafety.

3.4.3. *In vivo antibacterial activity*

Bone samples with implants from infected bone defect were harvested to evaluate the antibacterial performance both qualitatively and quantitatively (Fig. 9a and b). Large amounts of bacteria were isolated from both Zn–1Mg scaffold and surrounding bone tissue, whereas significantly less bacteria were found in PV/Zn–1Mg and HB/PV/Zn–1Mg. PV/Zn–1Mg and HB/PV/Zn–1Mg showed significantly stronger antibacterial performance than that of Zn–1Mg. H&E staining sections of the femoral condyle were performed to further evaluate the antibacterial performance (Fig. 9c). A large amount of inflammatory cell infiltration was found in the infected lesions of Zn–1Mg, and a small amount of sequestrum was observed. In contrast, *S. aureus*-induced infection in PV/Zn–1Mg and HB/PV/Zn–1Mg was controlled, with only a small amount of inflammatory cell infiltration and no obvious sequestrum.

4. Discussion

4.1. *Biodegradation behavior*

It is of great importance to adjust the degradation behavior of biodegradable bone implants to match the bone remodeling process. Zn alloys show a totally different degradation behavior compared with Mg alloys, which are widely reported in current studies [28–39]. In general, the degradation rate of Mg alloys is significantly high, leading to the loss of mechanical integrity in the early stage of bone repair. The degradation rate of Zn alloy is 1–12 times slower than that of Mg, effectively avoiding the early failure of implant caused by the fast degradation [35]. In physiological environments, Zn alloys are majorly degraded by anodic oxidation of Zn to Zn^{2+} and cathodic reduction of oxygen, resulting in the formation of ZnO and $Zn(OH)_2$ passivation layers, which effectively protect the matrix in the further corrosion process [54]. Subsequently, abundant chloride ions in the physiological media destroy the passivation layer and convert it into soluble salts, such as hydrated zinc phosphate [55,56], which is confirmed in immersion test in this study. The corrosion products of porous Zn–1Mg scaffolds were mainly composed of Zn, Mg, Ca and P, indicating the presence of calciate, phosphates and oxides of Zn or Mg (Fig. 3b). Different degradation behaviors result in the formation of different kinds and amounts of corrosion products. Corrosion products play an important role in biocompatibility. The corrosion products of Zn alloys mainly included Zn^{2+}, hydroxide ions, oxides and Ca/P compounds. Appropriate

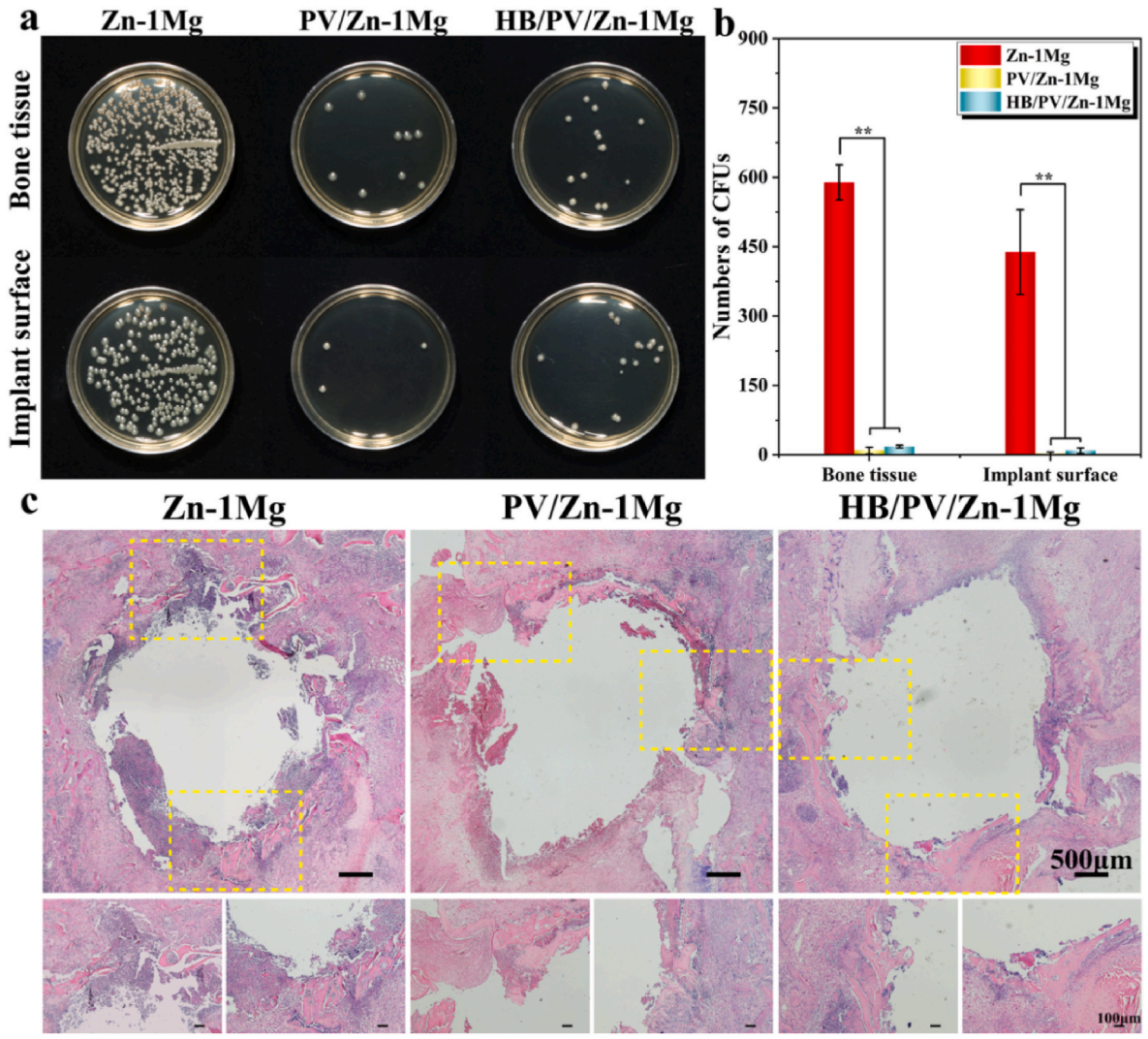

Fig. 9. In vivo antibacterial activity: (a, b) Representative images and number of bacterial colonies of bacterial cultures obtained in the peri-implanted bone tissues and on the surface of implants; (c) H&E staining slices of the infected femoral condyle.

concentrations of corrosion products can have beneficial effects on the host response, whereas excessive concentrations of corrosion products accumulation may disturb the local physiological equilibrium at the implantation site, and resulting in adverse effects on the surrounding tissue [43]. Therefore, the modulation of degradation behavior of Zn alloys can directly adjust the biocompatibility of Zn-based implants.

Our previous study showed that the degradation rate of AM porous Zn–Mg alloy increases with the increase of Mg element content [42]. This was attributed to the increase of Mg-rich phases in Zn–Mg alloy. The preferential degradation of Mg generates corrosion products $Mg(OH)_2$ with limited passivation effect, which resulted to a faster degradation and more release of metal ions. Moreover, the high specific area, resulted from the rough surface and the interconnected pores of AM porous Zn–Mg scaffolds, also increased the degradation rate due to the enlarged contact surface exposed to corrosive medium. Considering the healing time of bones, implants should maintain mechanical integrity within the body for a period of 3–6 months [57]. Nevertheless, the complete degradation of Zn alloys in the body takes 20 months or even longer [36]. Therefore, to accelerate degradation, alloying and porous structure design can be adopted. However, when the degradation rate is high, for Zn–Mg alloy orthopedic implants, the excessive release of Zn^{2+} has negative effects on cells and tissues [44]. Hence, in order to avoid the excessive release of Zn^{2+}, during the stage of bone remodeling, the degradation rate of the Zn–Mg alloy should be well controlled, so that the concentration of Zn^{2+} is within the threshold that is favorable for bone repair. After the completion of the bone repair, the residual Zn–Mg implant should be degraded at an accelerated rate to shorten the retention time of the implant.

Surface coating is an effective strategy to control the early rapid degradation of bone implants [58]. By physically blocking the corrosive medium, the coating can significantly decrease the corrosion rate of substrate and its protective effect disappears after shedding or degradation. PDA and HA have been utilized to deposit barrier layer with well-defined thickness and uniform conformity on the surface of 3D porous scaffolds [59]. Lin et al. developed HA/PDA composite coatings on the surface of Mg alloys by PDA inducing biomimetic mineralization in CaP solution. The corrosion resistance of modified Mg alloys significantly increased, and the modified alloy induce no toxic effects [52]. In this study, the HA/PDA barrier layer effectively inhibited the direct contact between corrosion medium and substrate. Therefore, the corrosion resistance of AM Zn–1Mg porous scaffolds was significantly improved after being coated with HA/PDA (Fig. 3). With corrosion proceeding, the corrosion medium gradually permeates through the nanogaps in the PDA and HA barrier layers and reacts slowly with the substrate. Finally, PDA and HA coatings will be corroded and damaged, failing to provide effective protection. The retarding corrosion effect of the coating offers the possibility for improving the tissue compatibility of porous Zn–Mg alloy. Otherwise, after the peeling of coating, the high

surface area of porous Zn–Mg alloy and the micro-galvanic corrosion between Mg-rich phase and Zn substrate can accelerate the corrosion of the Zn–Mg alloy, shortening the residence time of the Zn–Mg alloy [29,39,42]. The degradation behavior of coated scaffolds can be well controlled by adjusting critical factors of coatings, such as the coating thickness, structural density of the coating, and its bonding strength with the matrix, which can be adjusted by processing parameters for coating preparation. Although this study confirmed the corrosion retarding effect of HA/PDA composite coating, the precise control of corrosion behaviors by adjusting critical factors of coatings had not been investigated. Moreover, the peeling of coating and subsequent accelerated degradation was not observed. Therefore, in the future, more works need to be done to implement the customization of the degradation behaviors of Zn–Mg alloy scaffolds during different stages of bone repair.

4.2. Biocompatibility and osteogenic activity

A biphasic effect of Zn^{2+} on the MC3T3-E1 cells was observed (Fig. 4). Low concentrations of Zn^{2+} promoted the functionalization of osteogenic precursor cells. However, high concentrations of Zn^{2+} exhibited significant cytotoxicity due to stimulated cell injury/death. Yuan et al. found that Zn^{2+} could stimulate the growth and apoptosis of osteoblast-like cell simultaneously, and the process of cell apoptosis was dominant at high Zn^{2+} concentration [37], which was consistent with the results in our research. Sensi et al. also confirmed that high-dose Zn^{2+} could reversibly interfere electron transport in uncoupled mitochondria, and resulting in cellular damage [60]. Delayed osseointegration was also observed *in vivo*, after the implantation of Zn alloy scaffold, due to the local high concentration of Zn^{2+} [61]. For Zn–Mg alloy, the concentration of released Mg^{2+} also affected the cytocompatibility. The concentration threshold of Mg^{2+}, causing cytotoxicity, was much higher than that of Zn^{2+}. Reportedly, low-dose Mg^{2+} (<100 μg/ml) showed no cytotoxicity, and the cell viability was above 80%. While, it could induce obvious cell death when Mg^{2+} concentration was greater than 300 μg/mL [62]. In this study, the concentration of Mg^{2+} in all sample extracts was less than 100 μg/mL (Fig. 4c), indicating Mg^{2+} in extracts induced no cytotoxicity. Hence, the cytotoxicity was resulted from high concentration Zn^{2+}.

The best biocompatibility was observed in HB/PV/Zn–1Mg. The effect of Zn^{2+} on cell compatibility is dose-dependent, the low-concentration release of Zn^{2+} resulted from the HA/PDA composite coating significantly improves biocompatibility. In addition, the BMP2 loaded by composite coating also plays a vital role in promoting biocompatibility. BMP2 is a well-characterized cytokin with osteoinductive activity, which has been approved by FDA for clinical applications, and occupies an important position in the field of bone tissue engineering [63]. The exogenous BMPs can induce osteogenesis through blood-derived mesenchymal stem cells *in vivo*. According to Fig. 4c, the Zn^{2+} concentrations in the extracts of the HB/PV/Zn–1Mg group diluted 1-fold, were similar to those in the extracts of the other two groups of samples diluted 2-fold. However, a greater improvement of cell viability and osteogenic differentiation ability were observed in the cells co-cultured with diluted 1-fold extracts of HB/PV/Zn–1Mg group (Figs. 4 and 5). This clearly indicated that BMP2 released from the coatings significantly promoted the cytocompatibility of the coated Zn–1Mg scaffold. And the released BMP2 has a greater effect on the improvement of osteogenic capability compared to low concentrations of Zn^{2+}. Moreover, HA coating can improve the osteo-conductivity, and Ca, P ions in HA coating are beneficial for bone mineralization [64]. PDA coating has good biocompatibility and can promote osteoblast adhesion and proliferation by chelating Ca^{2+} through the catecholamine group, also increasing ALP activity [65,66].

According to the *in vivo* investigation, at week 12 after the surgery, significantly better bone healing and osseointegration were observed in HB/PV/Zn–1Mg, compared to Zn–1Mg (Figs. 7 and 8). In the early stage after implantation, tissue trauma leads to more accumulation of body fluids. Cells from peripheral and intramedullary blood and bone marrow cells generate a hematoma, accompanied by an acute inflammatory response [67]. The degradation rate of Zn–1Mg scaffold is high during this period, indicating the release of high amount of Zn^{2+}, which is detrimental to the functionalization of osteoblasts *in vivo*. For HB/PV/Zn–1Mg and PV/Zn–1Mg, HA and PDA coatings isolate the Zn–1Mg matrix from body fluids, thereby delaying the release of Zn^{2+}, significantly improving the bone repair. Furthermore, physicochemical properties of the modified Zn–1Mg scaffold surface also have a significant impact on the bone generation. After coating treatment, the improved wettability of the Zn–1Mg scaffold was observed (Fig. 2h). The surface hydrophilicity of bone repair materials is closely related to their biocompatibility and cell adhesion. PDA coatings contain a large number of hydrophilic groups, including hydroxyl and amino groups, which can bind to hydrophobic surface to improve the hydrophilicity, thus improving osteoblast adhesion, migration and functionalization *in vivo* [68]. In addition, the nanoscale roughness and high hydrophilicity of HA coatings can also improve the biological activity of implants [69]. To sum up, the improved biocompatibility of HB/PV/Zn–1Mg can be explained by the slow release of Zn^{2+}, the existence of HA and PDA, and the co-stimulation of exogenous BMP2.

4.3. Antibacterial property

For orthopedic implants, biomedical device-associated infections (BAI) caused by bacteria have always been a significant challenge [70,71]. Severe BAI is a devastating complication that can lead to pain, implant repair failure, systemic illness, loss of function and even death [72]. One of the typical characteristics of Zn alloys is the antibacterial effect. The antibacterial activity of Zn alloy is resulted from the ability of Zn^{2+} to induce oxidative stress. Zn^{2+} can interact with the thiol group of bacterial respiratory enzymes and inhibit their function, generating reactive oxygen species (ROS) and free radicals, which in turn irreversibly damaging bacterial cell walls, DNA and mitochondria, resulting in the death of bacterial cells [73,74]. High concentrations of Zn^{2+} indicate strong antibacterial effect but low osteogenic activity. In addition, when faced with a severe clinical infection, the antibacterial effect of Zn-based BMs alone is not enough to not completely inhibit bacterial growth. To enhance the antibacterial properties of Zn alloy implants, Zn–Cu or Zn–Ag alloys with strong antibacterial activity have been developed [75–77]. Through the co-release of Cu^{2+} or Ag^{+} with Zn^{2+}, Zn alloys inhibit the biosynthesis of bacterial toxins and the formation of bacterial biofilms. However, the potential cytotoxicity of Cu^{2+} and Ag^{+} is a concern for clinical applications [78,79].

The antibacterial functionalization of the implant surface is an effective strategy to reduce the incidence of BAI [72]. In this study, the antibacterial drug Van was loaded into PDA coating by in situ self-assembly. Compared with Zn–1Mg, an enhanced antibacterial effect on the gram-positive and negative bacteria was observed in PV/Zn–1Mg and HB/PV/Zn–1Mg (Figs. 6 and 9). The PDA coating loaded with Van can inhibit the formation of biofilm by killing adherent bacteria on the surface, and resist infection at the implantation site by sustained local drug release. Therefore, although the release of Zn^{2+} decreased due to the existence of coating, the enhanced antibacterial activity was shown in scaffolds resulted from the loaded antibacterial drug. Furthermore, the stronger antibacterial activity was observed for PV/Zn–1Mg compared to HB/PV/Zn–1Mg (Fig. 6a and b). This could be explained by the fact that during the preparation of HA coatings, the Van loaded by the PV/Zn–1Mg sample would be partially released into the HA deposition solution, where a part of Van co-deposited with HA and another part of Van lost. In addition, the HA coating would act as a barrier layer, causing the slow release of Van from the PDA coating. As shown in Fig. 2f and g, this reduction in the amount and rate of drug release was the main reason for the decrease in the antibacterial rate of HB/PV/Zn–1Mg. Some studies have shown that high concentrations of

antibiotics can inhibit osteoblast differentiation [80], and induce cellular mitochondrial dysfunction and oxidative damage, resulting in toxicity to mammalian cells [81]. The topical application of Van at the infection site has been shown effective and safe, avoiding potential toxic systemic effects, and showing less toxic to osteoblasts than other antibiotics such as cefazolin [82,83]. The toxicity caused by the drug-loaded coating, is greatly resulted from the instantaneous high concentration of antibiotics due to the drug burst release. The sustained and controlled release strategies for drug-loaded coating are major approaches to solve this concern. In the present study, PDA coating loaded with Van exhibited no toxic effects *in vitro* and *in vivo* tests, which could be due to the fact that Van released from PV/Zn–1Mg and HB/PV/Zn–1Mg was always maintained at a low concentration (Fig. 2f and g).

Overall, this work confirms the feasibility and satisfactory effect of a multifunctional design of AM Zn–1Mg porous scaffold by drug-loaded coatings. Meanwhile, the coating also provides greater freedom to regulate the degradation rate of the Zn–Mg alloy scaffold. However, how to precisely match the degradation behavior of Zn–Mg alloy porous scaffolds to match the bone repair needs in the spatio-temporal dimensions still needs to be studied in various aspects such as zinc alloy composition, pore structure design and coating modification. Besides, longer-term *in vivo* investigations are also necessary, especially on the metabolic mechanism of Zn^{2+} *in vivo* and its affects. Also, more multifunctional designs should be attempted to be investigated, including immunomodulation and angiogenesis, because of their important role in bone repair processes. We will also conduct more investigations on specific pathological models to facilitate the clinical translation of porous Zn–Mg alloy scaffolds with multifunctional design.

5. Conclusions

In this study, the HA/PDA composite coating loaded with drugs was successfully prepared on Zn–1Mg porous scaffold to control biodegradation, and locally deliver antibacterial drug and osteogenic growth factor to improve antibacterial and osteogenic properties. The degradation behavior, biocompatibility, osteogenic and antibacterial activities were systematically investigated. The main conclusions were as follows.

(1) The HA/PDA composite coating immobilized BMP2 and Van stably and maintained their long-lasting release. The HA/PDA composite coating retarded the corrosion of porous Zn–1Mg due to the effect of physical barrier.
(2) The HA/PDA composite coating loaded with BMP2 significantly improved biocompatibility and osteogenic activity *in vitro* and *in vivo*, which was attributed to the immobilization of BMP2 synergistically with low concentration of Zn^{2+}. Meanwhile, the change of physicochemical properties on the surface of Zn–1Mg scaffold also promoted osseointegration *in vivo*.
(3) The PDA coating loaded with Van showed a high antibacterial capacity, killed gram-positive and negative bacteria through the sustained release of Van, and endowed Zn–1Mg scaffolds with stronger antibacterial activity.

Data availability

The data that support the findings of this article are available from the corresponding author upon reasonable request.

CRediT authorship contribution statement

Zhenbao Zhang: Conceptualization, Investigation, Data curation, Writing – original draft. **Aobo Liu:** Investigation, Data curation, Writing – original draft. **Jiadong Fan:** Investigation, Writing – original draft. **Menglin Wang:** Investigation, Data curation. **Jiabao Dai:** Structure design, Data curation. **Xiang Jin:** Investigation. **Huanze Deng:** Investigation. **Xuan Wang:** Investigation. **Yijie Liang:** Data curation. **Haixia Li:** CT scan. **Yantao Zhao:** Supervision, Resources. **Peng Wen:** Supervision, Resources, Writing – review & editing. **Yanfeng Li:** Supervision, Resources, Writing – review & editing.

Declaration of competing interest

The authors declare that they have no known competing financial interests or personal relationships that could have appeared to influence the work reported in this paper.

Acknowledgments

This work was funded by National Natural Science Foundation of China (52175274, 51875310, 82151312 and 82272493), Beijing Natural Science Foundation (L222110, L212067), Capital's Funds for Health Improvement and Research (CFH2020-2-5021), Open Project of state key laboratory of military stomatology (2019KA01) and Key Military Medical Projects (BLB20J001). The author was thankful for the financial support of Residency Training Quality Improvement Program from Beijing Municipal Health Commission.

Appendix A. Supplementary data

Supplementary data to this article can be found online at https://doi.org/10.1016/j.bioactmat.2023.04.017.

References

[1] T. Winkler, F.A. Sass, G.N. Duda, K. Schmidt-Bleek, A review of biomaterials in bone defect healing, remaining shortcomings and future opportunities for bone tissue engineering: the unsolved challenge, Bone Joint Res 7 (3) (2018) 232–243.
[2] Y. Sun, H.L. Wu, W.H. Wang, R. Zan, H.Z. Peng, S.X. Zhang, X.N. Zhang, Translational status of biomedical Mg devices in China, Bioact. Mater. 4 (2019) 358–365.
[3] J.Z. Zhang, Y.B. Jiang, Z.Z. Shang, B. Zhao, M.Y. Jiao, W.B. Liu, M.B. Cheng, B. Zhai, Y.J. Guo, B. Liu, X.L. Shi, B. Ma, Biodegradable metals for bone defect repair: a systematic review and meta-analysis based on animal studies, Bioact. Mater. 6 (11) (2021) 4027–4052.
[4] K.J. Burg, S. Porter, J.F. Kellam, Biomaterial developments for bone tissue engineering, Biomaterials 21 (23) (2000) 2347–2359.
[5] Q.Z. Chen, C.H. Zhu, G.A. Thouas, Progress and challenges in biomaterials used for bone tissue engineering: bioactive glasses and elastomeric composites, Prog Biomater 1 (1) (2012) 2.
[6] T. Miyazaki, K. Ishikawa, Y. Shirosaki, C. Ohtsuki, Organic-inorganic composites designed for biomedical applications, Biol. Pharm. Bull. 36 (11) (2013) 1670–1675.
[7] R.B. Minkowitz, S. Bhadsavle, M. Walsh, K.A. Egol, Removal of painful orthopaedic implants after fracture union, J Bone Joint Surg Am 89 (9) (2007) 1906–1912.
[8] Y. Liu, Y.F. Zheng, X.H. Chen, J.A. Yang, H.B. Pan, D.F. Chen, L.N. Wang, J. L. Zhang, D.H. Zhu, S.L. Wu, K.W.K. Yeung, R.C. Zeng, Y. Han, S.K. Guan, Fundamental theory of biodegradable metals-definition, criteria, and design, Adv. Funct. Mater. 29 (18) (2019), 1805402.
[9] X. Tong, D.C. Zhang, X.T. Zhang, Y.C. Su, Z.M. Shi, K. Wang, J.G. Lin, Y.C. Li, J. X. Lin, C. Wen, Microstructure, mechanical properties, biocompatibility, and in vitro corrosion and degradation behavior of a new Zn-5Ge alloy for biodegradable implant materials, Acta Biomater. 82 (2018) 197–204.
[10] P. Xiong, J.L. Yan, P. Wang, Z.J. Jia, W.H. Zhou, W. Yuan, Y.Y. Li, Y. Liu, Y. Cheng, D.F. Chen, Y.F. Zheng, A pH-sensitive self-healing coating for biodegradable magnesium implants, Acta Biomater. 98 (2019) 160–173.
[11] N. Zhang, W.D. Wang, X.Z. Zhang, K.C. Nune, Y. Zhao, N. Liu, R.D.K. Misra, K. Yang, L.L. Tan, J.L. Yan, The effect of different coatings on bone response and degradation behavior of porous magnesium-strontium devices in segmental defect regeneration, Bioact. Mater. 6 (6) (2020) 1765–1776.
[12] M. Li, P. He, Y.H. Wu, Y. Zhang, H. Xia, Y.F. Zheng, Y. Han, Stimulatory effects of the degradation products from Mg-Ca-Sr alloy on the osteogenesis through regulating ERK signaling pathway, Sci. Rep. 6 (2016), 32323.
[13] G.Y. Li, L. Zhang, L. Wang, G.Y. Yuan, K.R. Dai, J. Pei, Y.Q. Hao, Dual modulation of bone formation and resorption with zoledronic acid-loaded biodegradable magnesium alloy implants improves osteoporotic fracture healing: an in vitro and in vivo study, Acta Biomater. 65 (2018) 486–500.
[14] W. Wang, G.Z. Jia, Q. Wang, H. Huang, X.L. Li, H. Zeng, W.J. Ding, F. Witte, C. Q. Zhang, W.T. Jia, G.Y. Yuan, The in vitro and in vivo biological effects and osteogenic activity of novel biodegradable porous Mg alloy scaffolds, Mater. Des. 189 (2020), 108514.

[15] M.N. Sarian, N. Iqbal, P. Sotoudehbagha, M. Razavi, Q.U. Ahmed, C. Sukotjo, H. Hermawan, Potential bioactive coating system for high-performance absorbable magnesium bone implants, Bioact. Mater. 12 (2021) 42–63.
[16] D. Bian, W.R. Zhou, Y. Liu, N. Li, Y.F. Zheng, Z.L. Sun, Fatigue behaviors of HP-Mg, Mg-Ca and Mg-Zn-Ca biodegradable metals in air and simulated body fluid, Acta Biomater. 41 (2016) 351–360.
[17] C.L Li, X.H Yao, R.Q Hang, Facile Preparation of Nanostructured Octacalcium Phosphate Coatings on Micro-arc Oxidized Magnesium with Different Functionalities for Bone Repair Application, Colloids Surf B Biointerfaces 197 (2021) 111426.
[18] B.Y. Sui, H. Lu, X. Liu, J. Sun, High-purity Mg and Mg-1Ca alloys: comparative assessment of the merits regarding degradation, osteogenesis, and biosafety for orthopedic applications, J. Mater. Sci. Technol. 140 (2023) 58–66.
[19] Y.W. Yang, C.F. Lu, S.P. Peng, L.D. Shen, D. Wang, F.W. Qi, C.J. Shuai, Laser additive manufacturing of Mg-based composite with improved degradation behaviour, Virtual Phys. Prototyp. 15 (3) (2020) 278–293.
[20] Y.W. Yang, C.F. Lu, L.D. Shen, Z.Y. Zhao, S.P. Peng, C.J. Shuai, In-situ deposition of apatite layer to protect Mg-based composite fabricated via laser additive manufacturing, J. Magnesium Alloys 11 (2) (2023) 629–640.
[21] R.H. Yao, S.Y. Han, Y.H. Sun, Y.Y. Zhao, R.F. Shan, L. Liu, X.H. Yao, R.Q. Hang, Fabrication and characterization of biodegradable Zn scaffold by vacuum heating-press sintering for bone repair, Biomater Adv 138 (2022), 212968.
[22] H.Z. Wu, X.X. Xie, J. Wang, G.Z. Ke, H. Huang, Y. Liao, Q.Q. Kong, Biological properties of Zn-0.04Mg-2Ag: a new degradable zinc alloy scaffold for repairing large-scale bone defects, J. Mater. Res. Technol. 13 (2021) 1779–1789.
[23] X. Wang, X.X. Shao, T.Q. Dai, F.F. Xu, J.G. Zhou, G.Q. Qu, L. Tian, B. Liu, Y.P. Liu, In vivo study of the efficacy, biosafety, and degradation of a zinc alloy osteosynthesis system, Acta Biomater. 92 (2019) 351–361.
[24] D.D. Xia, F. Yang, Y.F. Zheng, Y.S. Liu, Y.S. Zhou, Research status of biodegradable metals designed for oral and maxillofacial applications: a review, Bioact. Mater. 6 (11) (2021) 4186–4208.
[25] H. Guo, D.D. Xia, Y.F. Zheng, Y. Zhu, Y.S. Liu, Y.S. Zhou, A pure zinc membrane with degradability and osteogenesis promotion for guided bone regeneration: in vitro and in vivo studies, Acta Biomater. 106 (2020) 396–409.
[26] D. Chen, L.C. Waite, W.M. P Jr., In vitro effects of zinc on markers of bone formation, Biol. Trace Elem. Res. 68 (3) (1999) 225–234.
[27] X.K. Fu, Y.Y. Li, T.L. Huang, Z.W. Yu, K. Ma, M. Yang, Q.L. Liu, H.B. Pan, H. Y. Wang, J.F. Wang, M. Guan, Runx2/Osterix and zinc uptake synergize to orchestrate osteogenic differentiation and citrate containing bone apatite formation, Adv. Sci. 5 (4) (2018), 1700755.
[28] Z.C. Zhang, B. Jia, H.T. Yan, Y. Han, Q. Wu, K.R. Dai, Y.F. Zheng, Biodegradable ZnLiCa ternary alloys for critical-sized bone defect regeneration at load-bearing sites: in vitro and in vivo studies, Bioact. Mater. 6 (11) (2021) 3999–4013.
[29] H.T. Yang, X.H. Qu, W.J. Lin, D.F. Chen, D.H. Zhu, K.R. Dai, Y.F. Zheng, Enhanced osseointegration of Zn-Mg composites by tuning the release of Zn ions with sacrificial Mg-rich anode design, ACS Biomater. Sci. Eng. 5 (2) (2019) 453–467.
[30] R.M. Li, Y.T. Ding, H.F. Zhang, J. Lei, Y. Shen, Effective strengthening and toughening in Zn-1Mg alloy with bimodal grain structure achieved by conventional extrusion, Mat Sci Eng A-Struct 854 (2022), 143850.
[31] Y.L. Zou, X. Chen, B. Chen, Effects of Ca concentration on degradation behavior of Zn-xCa alloys in Hank's solution, Mater. Lett. (2018) 193–196.
[32] B. Jia, H.T. Yang, Z.C. Zhang, X.H. Qu, X.F. Jia, Q. Wu, Y. Han, Y.F. Zheng, K. R. Dai, Biodegradable Zn-Sr alloy for bone regeneration in rat femoral condyle defect model: in vitro and in vivo studies, Bioact. Mater. 6 (6) (2020) 1588–1604.
[33] H.T. Yang, X.H. Qu, M.Q. Wang, H.W. Cheng, B. Jia, J.F. Nie, K.R. Dai, Y.F. Zheng, Zn-0.4Li alloy shows great potential for the fixation and healing of bone fractures at load-bearing sites, Chem Eng J 417 (2021), 129317.
[34] B. Jia, H.T. Yang, Y. Han, Z.C. Zhang, X.H. Qu, Y.F. Zhuang, Q. Wu, Y.F. Zheng, K. R. Dai, In vitro and in vivo studies of Zn-Mn biodegradable metals designed for orthopedic applications, Acta Biomater. 108 (2020) 358–372.
[35] H.T. Yang, B. Jia, Z.C. Zhang, X.H. Qu, G.N. Li, W.J. Lin, D.H. Zhu, K.R. Dai, Y. F. Zheng, Alloying design of biodegradable zinc as promising bone implants for load-bearing applications, Nat. Commun. 11 (1) (2020) 401.
[36] A.J. Drelich, S. Zhao, R.J. Guillory, J.W. Drelich, J. Goldman, Long-term surveillance of zinc implant in murine artery: surprisingly steady biocorrosion rate, Acta Biomater. 58 (2017) 539–549.
[37] W. Yuan, B. Li, D.F. Chen, D.H. Zhu, Y. Han, Y.F. Zheng, Formation mechanism, corrosion behavior, and cytocompatibility of microarc oxidation coating on absorbable high-purity zinc, ACS Biomater. Sci. Eng. 5 (2) (2019) 487–497.
[38] Y. Qin, P. Wen, H. Guo, D.D. Xia, Y.F. Zheng, L. Jauer, R. Poprawe, M. Voshage, J. H. Schleifenbaum, Additive manufacturing of biodegradable metals: current research status and future perspectives, Acta Biomater. 98 (2019) 3–22.
[39] Y Qin, H.T Yang, A.B Liu, J.B Dai, P Wen, Y.F Zheng, Y Tian, S Li, Processing Optimization, Mechanical Properties, Corrosion Behavior and Cytocompatibility of Additively Manufactured Zn-0.7Li Biodegradable Metals, Acta Biomater. 142 (2022) 388–401.
[40] K. Vassilis, K. David, Porosity of 3D biomaterial scaffolds and osteogenesis, Biomaterials 26 (27) (2005) 5474–5491.
[41] P. Wen, M. Voshage, L. Jauer, Y.Z. Chen, Y. Qin, R. Poprawe, J.H. Schleifenbaum, Laser additive manufacturing of Zn metal parts for biodegradable applications: processing, formation quality and mechanical properties, Mater. Des. 155 (2018) 36–45.
[42] Y. Qin, A.B. Liu, H. Guo, Y.N. Shen, P. Wen, H. Lin, D.D. Xia, M. Voshage, Y. Tian, Y.F. Zheng, Additive manufacturing of Zn-Mg alloy porous scaffolds with enhanced osseointegration: in vitro and in vivo studies, Acta Biomater. 145 (2022) 403–415.
[43] D.D. Xia, Y. Qin, H. Guo, P. Wen, H. Lin, M. Voshage, J.H. Schleifenbaum, Y. Cheng, Y.F. Zheng, Additively manufactured pure zinc porous scaffolds for critical-sized bone defects of rabbit femur, Bioact. Mater. 19 (2022) 12–23.
[44] J. Kubasek, D. Vojtech, E. Jablonska, I. Pospisilova, J. Lipov, T. Ruml, Structure, mechanical characteristics and in vitro degradation, cytotoxicity, genotoxicity and mutagenicity of novel biodegradable Zn-Mg alloys, Mater Sci Eng C Mater Biol Appl 58 (2016) 24–35.
[45] H.F. Qiang, Z.Y. Lv, C.Y. Hou, X. Luo, J. Li, K. Liu, C.X. Meng, W.Q. Du, Y.J. Zhang, X.M. Chen, F.Z. Liu, Development of biodegradable Zn-Mn-Li and CaP coatings on Zn-Mn-Li alloys and cytocompatibility evaluation for bone graft, Front. Bioeng. Biotechnol. 10 (2022), 1013097.
[46] W. Yuan, D.D. Xia, Y.F. Zheng, X.M. Liu, S.L. Wu, B. Li, Y. Han, Z.J. Jia, D.H. Zhu, L.Q. Ruan, K. Takashima, Y.S. Liu, Y.S. Zhou, Controllable biodegradation and enhanced osseointegration of ZrO2-nanofilm coated Zn-Li alloy: in vitro and in vivo studies, Acta Biomater. 105 (2020) 290–303.
[47] Y. Zhuang, Q.C. Liu, G.Z. Jia, H.L. Li, G.Y. Yuan, H.B. Yu, A biomimetic zinc alloy scaffold coated with brushite for enhanced cranial bone regeneration, ACS Biomater. Sci. Eng. 7 (3) (2021) 893–903.
[48] J.Y. Li, L.L. Li, J. Zhou, Z. Zhou, X.L. Wu, L.M. Wang, Q.Q. Yao, 3D printed dual-functional biomaterial with self-assembly micro-nano surface and enriched nano argentum for antibalctorial and bone regeneration, Appl. Mater. Today 17 (2019) 206–215.
[49] W. Cheng, X.W. Zeng, H.Z. Chen, Z.M. Li, W.F. Zeng, L. Mei, Y.L. Zhao, Versatile polydopamine platforms: synthesis and promising applications for surface modification and advanced nanomedicine, ACS Nano 13 (8) (2019) 8537–8565.
[50] Z.W. Zhou, B. Zheng, Y.P. Gu, C. Shen, J. Wen, Z.B. Meng, S.P. Chen, J. Ou, A. M. Qin, New approach for improving anticorrosion and biocompatibility of magnesium alloys via polydopamine intermediate layer-induced hydroxyapatite coating, Surface. Interfac. 19 (2020), 100501.
[51] S. Bose, S. Tarafder, Calcium phosphate ceramic systems in growth factor and drug delivery for bone tissue engineering: a review, Acta Biomater. 8 (4) (2012) 1401–1421.
[52] B.P. Lin, M. Zhong, C.D. Zheng, L. Cao, D.L. Wang, L.N. Wang, J. Liang, B.C. Cao, Preparation and characterization of dopamine-induced biomimetic hydroxyapatite coatings on the AZ31 magnesium alloy, Surf. Coat. Technol. 281 (2015) 82–88.
[53] C. Garcia-Mintegui, L.C. Cordoba, J. Buxadera-Palomero, A. Marquina, E. Jimenez-Pique, M.P. Ginebra, J.L. Cortina, M. Pegueroles, Zn-Mg and Zn-Cu alloys for stenting applications: from nanoscale mechanical characterization to in vitro degradation and biocompatibility, Bioact. Mater. 6 (12) (2021) 4430–4446.
[54] H.T. Yang, C. Wang, C.Q. Liu, H.W. Chen, Y.F. Wu, J.T. Han, Z.C. Jia, W.J. Lin, D. Y. Zhang, W.T. Li, W. Yuan, H. Guo, H.F. Li, G.X. Yang, D.L. Kong, D.H. Zhu, K. Takashima, L.Q. Ruan, J.F. Nie, X. Li, Y.F. Zheng, Evolution of the degradation mechanism of pure zinc stent in the one-year study of rabbit abdominal aorta model, Biomaterials 145 (2017) 92–105.
[55] M. Mouanga, P. Bercot, J.Y. Rauch, Comparison of corrosion behaviour of zinc in NaCl and in NaOH solutions. Part I: corrosion layer characterization, Corrosion Sci. 52 (12) (2010) 3984–3992.
[56] P.K. Bowen, J. Drelich, J. Goldman, Zinc exhibits ideal physiological corrosion behavior for bioabsorbable stents, Adv. Mater. 25 (18) (2013) 2577–2582.
[57] Y.F. Zheng, X.N. Gu, F. Witte, Biodegradable metals, Mater Sci Eng R 77 (2014) 1–34.
[58] S.V. Dorozhkin, Calcium orthophosphate coatings on magnesium and its biodegradable alloys, Acta Biomater. 10 (7) (2014) 2919–2934.
[59] Y. Li, W. Yang, X.K. Li, X. Zhang, C.R. Wang, X.F. Meng, Y.F. Pei, X.L. Fan, P. H. Lan, C.H. Wang, X.J. Li, Z. Guo, Improving osteointegration and osteogenesis of three-dimensional porous Ti6Al4V scaffolds by polydopamine-assisted biomimetic hydroxyapatite coating, ACS Appl. Mater. Interfaces 7 (10) (2015) 5715–5724.
[60] S.L. Sensi, D. Ton-That, P.G. Sullivan, E.A. Jonas, K.R. Gee, L.K. Kaczmarek, J. H. Weiss, Modulation of mitochondrial function by endogenous Zn2+ pools, Proc. Natl. Acad. Sci. U.S.A. 100 (10) (2003) 6157–6162.
[61] H.T. Yang, X.H. Qu, W.J. Lin, C. Wang, D.J. Zhu, D.R. Dai, Y.F. Zheng, In vitro and in vivo studies on zinc-hydroxyapatite composites as novel biodegradable metal matrix composite for orthopedic applications, Acta Biomater. 71 (2018) 200–214.
[62] Z. Zhen, X.L. Liu, T. Huang, T.F. Xi, Y.F. Zheng, Hemolysis and cytotoxicity mechanisms of biodegradable magnesium and its alloys, Mater Sci Eng C Mater Biol Appl 46 (2015) 202–206.
[63] M.M. Martino, P.S. Briquez, K. Maruyama, J.A. Hubbell, Extracellular matrix-inspired growth factor delivery systems for bone regeneration, Adv. Drug Deliv. Rev. 94 (2015) 41–52.
[64] J.X. Chen, Y. Yang, I.P. Etim, L.L. Tan, K. Yang, R.D.K. Misra, J.H. Wang, X.P. Su, Recent advances on development of hydroxyapatite coating on biodegradable magnesium alloys: a review, Materials 14 (19) (2021) 5550.
[65] S. Kim, C.B. Park, Mussel-inspired transformation of CaCO3 to bone minerals, Biomaterials 31 (25) (2010) 6628–6634.
[66] X. Xiao, Y. Xu, J.J. Fu, B. Gao, K.F. Huo, P.K. Chu, Enhanced hydroxyapatite growth and osteogenic activity on polydopamine coated Ti implants, Nanosci. Nanotechnol. Lett. 7 (3) (2015) 233–239.
[67] R. Marsell, T.A. Einhorn, The biology of fracture healing, Injury 42 (6) (2011) 551–555.
[68] J.H. Du, Y. Zhou, X.G. Bao, Z.R. Kang, J.M. Huang, G.H. Xu, C.Q. Yi, D.J. Li, Surface polydopamine modification of bone defect repair materials: characteristics and applications, Front. Bioeng. Biotechnol. 10 (2022), 974533.
[69] B. Yuan, H.W. Chen, R. Zhao, X.G. Deng, G. Chen, X. Yang, Z.W. Xiao, A. Aurora, B. A. Iulia, K. Zhang, X.D. Zhu, A.V. Iulian, S. Hai, X.D. Zhang, Construction of a magnesium hydroxide/graphene oxide/hydroxyapatite composite coating on Mg-

Ca-Zn-Ag alloy to inhibit bacterial infection and promote bone regeneration, Bioact. Mater. 18 (2022) 354–367.
[70] C.T. Johnson, A.J. Garcia, Scaffold-based anti-infection strategies in bone repair, Ann. Biomed. Eng. 43 (3) (2015) 515–528.
[71] B.H. Kapadia, R.A. Berg, J.A. Daley, J. Fritz, A. Bhave, M.A. Mont, Periprosthetic joint infection, Lancet 387 (10016) (2016) 386–394.
[72] Y.J. Sun, Y.Q. Zhao, Q. Zeng, Y.W. Wu, Y. Hu, S. Duan, Z.H. Tang, F.J. Xu, Dual-Functional implants with antibacterial and osteointegration-promoting performances, ACS Appl. Mater. Interfaces 11 (40) (2019) 36449–36457.
[73] P.K. Mishra, H. Mishra, A. Ekielski, S. Talegaonkar, B. Vaidya, Zinc oxide nanoparticles: a promising nanomaterial for biomedical applications, Drug Discov. Today 22 (12) (2017) 1825–1834.
[74] S. Dwivedi, R. Wahab, F. Khan, Y.K. Mishra, J. Musarrat, A.A. Al-Khedhairy, Reactive oxygen species mediated bacterial biofilm inhibition via zinc oxide nanoparticles and their statistical determination, PLoS One 9 (11) (2014), e111289.
[75] X.H. Qu, H.T. Yang, B. Jia, Z.F. Yu, Y.F. Zheng, K.R. Dai, Biodegradable Zn-Cu alloys show antibacterial activity against MRSA bone infection by inhibiting pathogen adhesion and biofilm formation, Acta Biomater. 117 (2020) 400–417.
[76] X.H. Qu, H.T. Yang, B. Jia, M.Q. Wang, B. Yue, Y.F. Zheng, K.R. Dai, Zinc alloy-based bone internal fixation screw with antibacterial and anti-osteolytic properties, Bioact. Mater. 6 (12) (2021) 4607–4624.
[77] B. Jia, Z.C. Zhang, Y.F. Zhuang, H.T. Yang, Y. Han, Q. Wu, X.F. Jia, Y.H. Yin, X. H. Qu, Y.F. Zheng, K.R. Dai, High-strength biodegradable zinc alloy implants with antibacterial and osteogenic properties for the treatment of MRSA-induced rat osteomyelitis, Biomaterials 287 (2022), 121663.
[78] J. Wu, L.Y. Wang, J. He, C.H. Zhu, In vitro cytotoxicity of Cu^{2+}, Zn^{2+}, Ag^{+} and their mixtures on primary human endometrial epithelial cells, Contraception 85 (5) (2012) 509–518.
[79] W.M. Elshahawy, I. Watanabe, P. Kramer, In vitro cytotoxicity evaluation of elemental ions released from different prosthodontic materials, Dent. Mater. 25 (12) (2009) 1551–1555.
[80] C.T. Johnson, A.J. García, Scaffold-based anti-infection strategies in bone repair, Ann. Biomed. Eng. 43 (3) (2015) 515–528.
[81] S. Kalghatgi, C.S. Spina, J.C. Costello, M. Liesa, J.R. Morones-Ramirez, S. Slomovic, A. Molina, O.S. Shirihai, J.J. Collins, Bactericidal antibiotics induce mitochondrial dysfunction and oxidative damage in Mammalian cells, Sci. Transl. Med. 5 (192) (2013), 192ra85.
[82] H.Y. Chiang, L.A. Herwaldt, A.E. Blevins, E. Cho, M.L. Schweizer, Effectiveness of local vancomycin powder to decrease surgical site infections: a meta-analysis, Spine J. 14 (3) (2014) 397–407.
[83] M.L. Edin, T. Miclau, G.E. Lester, R.W. Lindsey, L.E. Dahners, Effect of cefazolin and vancomycin on osteoblasts in vitro, Clin. Orthop. Relat. Res. 333 (1996) 245–251.